Controllable Double Gradient Bandgap Strategy Enables High Efficiency Solution-Processed Kesterite Solar Cells

Yunhai Zhao, Shuo Chen, Muhammad Ishaq, Michel Cathelinaud, Chang Yan, Hongli Ma, Ping Fan, Xianghua Zhang, Zhenghua Su, Guangxing Liang

Controllable Double Gradient Band-gap Strategy Enables High Efficiency Solution-Processed Kesterite Solar Cells

Yunhai Zhao, Shuo Chen, Muhammad Ishaq, Michel Cathelinaud, Chang Yan, Hongli Ma, Ping Fan, Xianghua Zhang, Zhenghua Su, Guangxing Liang**

Y. Zhao, S. Chen, M. Ishaq, P. Fan, Z. Su, G. Liang

Shenzhen Key Laboratory of Advanced Thin Films and Applications Key Laboratory of Optoelectronic Devices and Systems, College of Physics and Optoelectronic Engineering

Shenzhen University, Shenzhen 518060, P. R. China.
E-mail: zhsu@szu.edu.cn (Prof. Su) and lgx@szu.edu.cn (Prof. Liang)

C. Yan

Sustainable Energy and Environment Thrust, Jiangmen Laboratory of Carbon Science and Technology, The Hong Kong University of Science and Technology (Guangzhou), Guangzhou, 510000, China

Y. Zhao, M. Cathelinaud, H. Ma, X. Zhang

CNRS, ISCR (Institut des Sciences Chimiques de Rennes), UMR 6226

Université de Rennes

Rennes F-35000, France

Abstract: The double gradient band-gap absorber has the potential to enhance carrier collection, improve light collection efficiency, and make the performance of solar cells more competitive. However, achieving the double gradient band-gap structure is challenging due to the comparable diffusion rates of cations during high-temperature selenization in kesterite $Cu_2ZnSn(S,Se)_4$ (CZTSSe) films. Here, we have successfully achieved a double gradient band-gap in CZTSSe absorber by spin-coating the K_2S solution during the preparation process of the precursor film. The K_2S insertion serves as an additional S source for the absorber, and the high affinity energy of K-Se causes the position of the spin-coated K_2S solution locally Se rich and S poor. More importantly, the position of the band-gap minimum (notch) and the depth of the notch can be controlled by varying the concentration of K_2S solution and its deposition stage, thereby avoiding the electronic potential barrier produced by an inadvertent notch position and depth. In addition, the K-Se liquid phase expedites the selenization process to elimination of the fine grain layer. The champion CZTSSe device achieved an efficiency of 13.70%, indicating the potential of double gradient band-gap engineering for future development of high-efficiency kesterite solar cells.

Keywords

Kesterite, band-gap engineering, double gradient, efficiency

1. Introduction

The limited availability of fossil energy resources and the environmental devastation

they cause has made the development of green and renewable energy technology a focus of attention for the governments and research scientists around the world. As an inexhaustible and renewable energy, the development and utilization of solar energy is of tremendous scientific significance for addressing both energy challenges and environmental concerns. Thin-film photovoltaic (PV) technology offers more versatility than silicon-based PV technology owing to its compelling properties: light-weight, compatibility with flexible and rigid substrates, and compliance with opaque and translucent architectures. Some inorganic thin-film solar cells, such as $Cu(In,Ga)Se_2$ and CdTe, have reached advanced and mature technological levels, but their practical applications are still limited due to the high fabrication costs and relatively low element reserves.[1] The novel $Cu_2ZnSn(S,Se)_4$ (CZTSSe) devices are considered an alternative to CIGS and CdTe due to their abundant element storage and non-toxicity.

At present, the highest efficiency of CZTSSe is over 14%, which is still lower than that of CIGS (23.6%) and Shockley-Queisser (S-Q) limit of CZTSSe (≈31%).[1, 2] Researchers commonly agree that the larger open circuit voltage deficit ($V_{OC\text{-}def}$) and relatively lower fill factor (FF) are the main factors restraining the further development of CZTSSe.[3, 4] The undesirable performance of CZTSSe devices compared to CIGS results from the obvious band and potential fluctuations, short minority carrier lifetime, and severe defect-related bulk carrier recombination. In addition, due to poor band matching at the heterojunction interface and weakened electron diffusion to ITO in the quasi-neutral region (QNR) near the back interface, the excitons are prone to recombine

at the front and back interface, resulting in significant V_{OC} loss.

Since CZTSSe and CIGS have similar crystal structures and the same device structure, the mature technology and optimization strategies of CIGS are worthy of reference. Reviewing the development history of CIGS, the rapid improvement of CIGS efficiency can be attributed to three strategies: (1) Replacing In with congener Ga. The introduction of Ga facilitates the increase of the V_{OC} due to the fact that the E_g is proportional to the V_{OC}.[5, 6] The researchers tried adding Ga to CZTSSe and found that it eliminated defects, increased minority carrier lifetime and improved the electrical property of CZTSSe.[7, 8] (2) Alkali post-deposition treatment. Light alkali metal (Li, Na) tend to enter the grain and heavy alkali metal (Rb, Cs) often distribute at the grain boundary. For CZTSSe, the performance enhancement due to alkali metal incorporation is usually attributed to better crystallinity, the reduced grain boundary recombination and the increased P-type doping.[9-11] (3) Double gradient band-gap absorber. In the preparation of the CIGS absorber, the evaporation rate of different elements in the co-evaporation process can be finely regulated to obtain double gradient band-gap from the Mo electrode to the heterojunction, where the band-gap first decreases and then increases, which is called "V-shape double gradient band-gap structure".[12, 13]

The shrinking band-gap (E_g) from the back electrode to the absorber forms a back surface field (BSF), assisting electron transport to the p-n junction. It diminishes the probability of recombination of carriers at Mo electrode and boosts the short-circuit current density (J_{SC}). The minimum value of E_g (the notch) in the middle of the absorber can ensure the light absorption of CIGS and promote the J_{SC}. The gradually increasing

E_g from the notch to the p-n junction can ensure a large E_g value at the heterojunction interface, so as to obtain high V_{OC}.[6, 14] This double gradient band-gap structure enables the absorber to obtain both good electron transport characteristics and high V_{OC}, which results in a significant increase in CIGS device efficiency and is instructive for CZTSSe. Besides, it has been shown that the appropriate notch location and depth are crucial for efficiency improvement. A large front gradient (the gradient band gap structure from the notch position to the CdS front interface) forms an electron barrier, and the electrons generated inside the notch and deep in the absorber do not have enough thermal energy to overcome this barrier, resulting in carrier recombination that reduces V_{OC} and FF.[15] Till now, the most efficient CZTSSe device are obtained by solution method, a rapid high temperature selenization process is required to convert amorphous precursor film into crystalline absorber. This high-temperature selenization process exhibits a rapid element diffusion to obtain a uniform elemental distribution, making it challenging to finely regulate the element flux and obtain a gradient band-gap structure as in CIGS.[16, 17] At the same time, the fine grain layer caused by residual organic impurity during the process of selenization is an inherent shortcoming of the solution process. Recently, researchers have sightseen the gradient band-gap of CZTSSe, signifying that CZTSSe absorber films with single gradient band-gap (either in the front or back) can be achieved through the selenization-sulfurization process.[18] However, the selenization-sulfurization progress generally requires the simultaneous supply of sulfur and selenium powders, which have different reactivity and therefore can be difficult to control. Some cation doping can change the band-gap to obtain absorber with gradient

band-gap structure. For example, Ge doping can yield absorber with a back gradient because Ge tends to accumulate at the bottom of absorber.[19] Recently, it has been found that Cu^{+} and Cd^{2+} can undergo solid-state ion-exchange reaction by heterojunction annealing, and the absorber with front gradient can be obtained.[17] These strategies can alleviate the carrier recombination at the front interface or back interface to a certain extent. By preparing a nano-CZTS layer on the surface of the absorber, Du et al. obtained a CZTSSe device with a U-shape gradient band-gap structure with an efficiency of 9.9%;[20] by spin-coating CZTSSe precursor solutions with different Ag contents, Wu et al. obtained V-shape gradient band-gap CZTSSe devices with an efficiency of 11.2%, demonstrating the potential of CZTSSe devices with double gradient band-gap structure.[16] However, these processes are relatively complicated. To be competitive in the photovoltaic market, a simpler process must be found to reduce costs and labor. More importantly, it is vital to develop a controllable formation methodology to control the notch position and the front gradient size to obtain the ideal double gradient band-gap structure. Herein, we assert the development of a non-toxic and facile treatment method, which not only regulate the notch position and the front gradient size to obtain a double gradient band-gap absorber but also improve the grain growth process.

In this work, the controllable preparation of double gradient band-gap CZTSSe absorber was successfully achieved by simply spin-coating K_2S solution at different stages of precursor film preparation. This strategy enables the preparation of absorber with different notch positions and front gradient sizes, which greatly improves the

carrier transport performance of CZTSSe absorber. At the same time, the existence of K avoids the deeper defects that may result from the introduction of additional S. Our study comprehensively investigated the impact of K_2S on the microscopic morphology, band structure, electrical properties, and defect characteristics of CZTSSe devices. SIMS analysis showed a small notch of the S/(S+Se) in the optimized sample near the front interface, signifying the successful formation of the absorber film with double gradient band-gap. It is witnessed that the K_2S treatment adjusted the element distribution profile, improved the carrier transportation, thinned the fine grain layer, and reduced the defect density. Due to the high chemical affinity between K and Se, K_2Se_3 liquid phase is formed during the selenization process, which can improve the absorber crystallinity. The K^+ in the absorber layer can stabilize the Sn content by increasing the elemental diffusion rate, thus reducing the transition path through Sn-related defects and suppressing band-gap fluctuations and electrostatic potential fluctuations. Meanwhile, K_2S can react with Sn during selenization to form wide band-gap $K_2Sn_2S_5$ reducing carrier recombination at the grain boundary. Besides, by etching the absorber to different thicknesses and assembling the device for EQE analysis, we demonstrated the band-gap profile of the CZTSSe device intuitively for the first time. We are convinced that the introduction of K_2S at an optimized stage can obtain CZTSSe devices with double gradient band-gap. We are claiming a novel and cost-effective approach to report the highest power conversion efficiency (13.70%) for CZTSSe devices based on gradient band-gap absorber.

2. Result and discussion

Figure 1a illustrates the schematic of the preparation process for both the reference and the K_2S sample. Three different K_2S solution concentrations were selected, the K_2S layer were inserted at different positions in the precursor film, which are described in detail in the experimental section. For the convenience of expression, samples with K_2S layer were abbreviated as xL-K_2S. For example, 3L-K_2S represents inserted K_2S layer between the third and fourth CZTSSe precursor layer. The correspondence between xL-K_2S and sample label is shown in **Table 1**. The best result is obtained by inserting K_2S layer between the sixth and seventh precursor films (6L-K_2S).

To investigate the intrinsic reason affecting the device performance upon inserting K_2S layer insertion at different positions, the elemental distribution profile of samples A-M were analyzed by SEM-EDS. The K_2S layer was found significantly affecting the S distribution as the K_2S layer provides additional S. On the other hand, K reacts with Se so easily due to high affinity energy that the location of K_2S layer is relatively Se-rich and S-poor (Low S/(S+Se) ratio, as shown in Figure 1b, the S/(S+Se) is abbreviated as SSe).[21, 22] The SSe profile of sample A-M were shown in Figure 1c-e. The front side (left part) of the SSe profile corresponds to the surface of absorber, and the other side corresponds to the interface with Mo. After selenization, all samples showed a decrease in SSe near the position of the K_2S layer. Obviously, higher the concentration of the K_2S solution is, the more obvious decrease in SSe will be. The SSe profile of sample B, F, J (the yellow curves) obtained by spin-coating the K_2S solution on Mo back electrode are smaller at the back interface compare to sample A; the sample E, I, M (the green curves) which obtained by spin-coating K_2S solution on the precursor film surface show

earlier depletion of SSe at the front surface. The SSe profile of sample C, G, K (the violet curve) obtained by inserting K_2S layer between the third and fourth layer of the precursor film and sample D, H, L (the pink curve) obtained by inserting K_2S layer between the sixth and seventh layer of the precursor film show obvious notch near the position of K_2S layer. SSe is higher at the surface and bottom of the absorber and lower in the middle of the absorber, demonstrating a V-shape double gradient distribution of SSe. The double gradient distribution of SSe indicates that the band-gap of absorber is double gradient structure. The EDS analysis demonstrated that the change of the SSe gradient profile of the absorber is the result of the varying K_2S solution concentration and spin coating position. With the upward shift of the K_2S spin-coating position, the notch is brought closer to the surface; higher K_2S solution concentration led to an increased degree of localized S poor, corresponding to more obvious SSe notch. Thus, the shape of double gradient band-gap and notch depth can be controlled simply by changing the position of K_2S layer and the concentration of K_2S solution. This modification is attributed to the adjustment of elemental distribution of Se and S in the absorber by K_2S layer. Since the reaction of Se with K is prioritized compared to that of S with K during the film growth, the high affinity energy of K-Se can accelerate the selenization and lead to Se rich and S poor locally near the K_2S layer, and thus the SSe profile changes.[23] This reaction sequence results in the front and back side of the film holding high SSe ratio when the K_2S layer is inserted in the middle of the absorber, while the middle of the film has a characteristic notch with low SSe ratio, so that the absorber possesses a composition distribution of double gradient of SSe.

The performance of the CZTSSe samples with K_2S layer were all enhanced, benefiting from the gradient band-gap structure formation. It can be seen from Table 1 that no matter whether the concentration of K_2S solution is high or low, the device efficiency is higher when the K_2S layer is inserted between the sixth and seventh layer of the precursor film, signifying the formation of double gradient band-gap structure. The experimental results demonstrate that increasing the concentration of the K_2S solution from 0.01 to 0.05 M leads to a more pronounced local Se-rich and S-poor region. As a result, the sample H with a deeper SSe notch obtains a device efficiency of 13.70%. However, when the concentration of the solution is increased to 0.1 M, the SSe notch of the corresponding sample L is further deepened and the device efficiency decreases instead. For Cu-based thin-film solar cells, p-n junctions are formed between absorber and buffer layer, leading to valence band and conduction band bending (Figure 1f).[15] The CZTSSe is divided into majority carrier depletion space charge region (SCR) and quasi-neutral region (QNR). Incident light is absorbed and generates electron-hole pairs that are separated by the built-in electric field within the SCR. Electrons collection from the CZTSSe absorber is critical for maximizing conversion efficiency However, the band alignment at the heterojunction interface is often unsatisfactory, and the dynamics of electron diffusion into the ITO shrinks in the QNR near the back interface. As a result, electrons and holes tend to recombine at the front and back interface eventually leading to significant $V_{OC\text{-}def}$. The existence of K_2S layer adjusts the S and Se distribution of in the absorber resulting in a double gradient band-gap structure (Figure 1g): the gradually decreasing E_g from Mo electrode to the notch provided additional BSF to help electron

transport to the p-n junction, thus reducing the probability of carriers recombination at back interface; the notch of band-gap can ensure the light absorption of CZTSSe and enhance the J_{SC}; the gradually increasing band-gap from the notch to the front surface ensures a large band-gap value at the p-n junction interface, which results in a high V_{OC}.[21, 24, 25] Therefore, the device performance of sample H is substantially improved. Normally, electrons generated in the SCR can be collected efficiently due to the strong electric field. Yet, the width of SCR is significantly reduced when the solar cell is operating, so that a large front gradient will lead to the existence of an electron barrier.[15, 26] This potential barrier does not significantly affect the device performance at room temperature, since the thermal energy is sufficient for most electrons to overcome it.[27-29] Nevertheless, it still increases the carrier recombination and reduces the V_{OC} and FF of the device, which is one of the main reasons why sample L is not as good as sample H. This means that excessively pronounced gradient (Fig. 1h) can lead to a large notch at the conduct band edge (E_C) and become an electronic potential barrier. Electrons generated within the notch and deep in the absorber cannot hold enough thermal energy to overcome this barrier. Thus the too deep notch becomes a trap for capturing electrons and leads to enhanced recombination with holes in the valence band. Therefore, tuning the appropriate band-gap gradient profile of CZTSSe is essential to reduce the recombination and achieve high efficiency.

In addition, inserting K_2S layer after third layer also exhibited a gradient band-gap, but the inappropriate notch position prevented the transport of photogenerated electrons, thus limiting the PCE **(Figure S1**). If the front gradient starts at the edge of the SCR

(where the bandgap notch is located), it eliminates the potential barrier at zero bias by forming an electron barrier at positive bias. This affects electron transport and hamper device performance.[14, 15] Conversely, the front gradient originated at QNR (where the bandgap notch is situated) creates an electron transfer barrier at any bias voltage. This significantly reduces electron collection capability, leading to a decline in J_{SC}, *FF*, and overall PCE.[27, 30] For sample C, G and K, the band-gap notch is closer to the back interface, suggesting that the notch is located in the QNR, and the presence of the electronic barrier in this case hinders the device efficiency, so that the PCE can only be improved to a certain extent despite the double gradient band-gap structure.

Table 1 confirms that sample H has the highest device efficiency, and the depth profile of S and Se of sample A and sample H were analyzed using SIMS with more accuracy. For the convenience of expression, sample A and sample H are abbreviated as REF and K_2S sample onward. As shown in **Figure S2**, the distribution of S for both samples have a similar trend while the K_2S sample has a higher S concentration due to the contribution of K_2S layer. The absorber film is Se-rich at the bottom of REF sample, due to the higher Se content in the fine grain layer. This bottom Se-rich phenomenon is diminished in the K_2S film, where the Se distribution in the K_2S film is more uniform compared to the REF film. The acceleration of selenization is caused by the high chemical affinity between K and Se, therefore the distribution of Se in the absorber is changed.[21, 22] The SSe distribution was extracted from the atomic concentration depth distribution of Figure S2 and displayed in **Figure 2**a. The distribution of SSe from CdS interface to the back electrode of the REF sample is relatively uniform, signifying a

relatively uniform band-gap profile. The SSe profile of the K_2S sample, on the other hand, exhibits a V-shape double gradient distribution trend, lowering first and then ascending, from the CdS interface to the Mo electrode. The band-gap of the CZTSSe absorber is positively correlated with the SSe ratio, this double gradient SSe profile imply that the K_2S sample has a double gradient band-gap absorber.

To investigate the film structure and the band-gap variation at different depths, we etched the REF and K_2S absorber film to different thicknesses by magnetron sputtering method, and controlled the thickness of the etched film by controlling the sputtering power and sputtering time (the thickness of the original REF and K_2S absorber is about 1.2 μm). The step profiler was used to quantify the thickness of the etched samples, which were designated R1-R10 and K1-K10. Each sample's thickness difference for R1-R10 was around 100 nm, and the same is true for K1-K10. **Table S1** displays the correlation between sample counts and thicknesses. To investigate the structural depth profile for CZTSSe absorber, REF/K_2S, R2/K2, R5/K5, R7/K7 and R10/K10 films were selected for XRD (**Figure S3**), and the (112) diffraction peak of all samples were enlarged and shown in Figure 2c and d to observe the changes. Both type of samples showed a similar diffraction pattern, however the (112) diffraction peak position of K_2S samples exhibited a right shift due to the addition S provided by K_2S (Figure 2e). For K_2S sample, the (112) peak position of the un-etched film and K2 film is 27.48 and 27.43, the (112) peak position of the K_2S film shifted to the left. As the etching depth deepens, the (112) peak position of the K5, K7 and K10 films is shifted to larger angle. Initially the left and then the rightward shift of (112) diffraction peak of the etched K_2S

sample along the depth indicated a decreasing and then increasing SSe ratio profile. These findings authenticated that the SSe of the surface and bottom of the K_2S sample is higher than that the middle, indicating the formation of SSe gradient upon K_2S layer insertion. These results are consistent with the SEM-EDS and SIMS results.

The UPS data for REF, K_2S, and CdS films are illustrated in **Figure S4** and **S5**, and the calculation shows the conduction band offset (CBO) value at the p-n junction interface (CBO_{REF}=0.563 eV, CBO_{K_2S}=0.354 eV). The optimal range of CBO is 0-0.4 eV, an electronic barrier is formed when the CBO is greater than 0.4 eV which deteriorates the device efficiency.[31] The reduction of CBO due to the upward shift of the E_C of the K_2S sample favors the improvement of the electron transport at the heterojunction and the reduction of the interface recombination (Figure 2e).[31] Both SIMS and XRD data confirm that SSe is higher at the surface and bottom and lower in the middle of K_2S absorber. The shorter Sn-S bond moves the CBM higher by generating stronger repulsion than the Sn-Se bond, so the S/(S+Se)-based double gradient implies that most likely the conduction band is also double gradient.[32] To verify this conclusion, XPS measurements were performed on the R1-R10 and K1-K10 films to obtain the value of their valence band. The results are shown in **Figure S6** and **S7**. The R1-R10 and K1-K10 films were assembled into solar cells and tested EQE to obtain the E_g to show the whole band-gap profiles of the absorber more thoroughly (**Figure S8-S10**). The valence band and band-gap at different location of the REF and K_2S absorber are summarized in Table S1. The conduction band position corresponding to different thicknesses of absorber were calculated based on the XPS and EQE. Figure 2f shows the band-gap

profile of REF and K_2S sample, Figure 2g and h show the fluctuations of the E_C and E_V of REF and K_2S sample. The band-gaps at different location of REF did not reveal significant fluctuations, which is consistent with the results of the SSe profile in SIMS analysis. In contrast, the band-gap of the K_2S sample initially diminishes as the thickness of the film decreases, with a minimum value near about 200-500 nm from the upper surface of the absorber, and then the E_g of the film increases slightly as the thickness decreases. This result is consistent with the notch in the SSe near CdS interface in the SIMS analysis and also with the variation of the (112) peak position at the crystal plane in the XRD analysis. The band structure diagram illustrates the presence of a double gradient band-gap in the K_2S sample. The varying conduction band in double gradient and then the conduction band gradient near the back interface is able to create an additional electric field to help the free electrons drift toward the front junction. This contributes to the efficient collection of carriers, especially near-infrared photon energy.[14, 27] Meanwhile, there is a notch in the conduction band position near the front interface, which improves the absorption of low-energy photons. The conduction band front gradient located within the space charge region helps to reduce the CBO and increase the V_{OC}.

Figure 3a shows the comparison of the performance of REF device and K_2S device. It is clear that the EQE response of the K_2S device is significantly increased in the 700-900 nm range compared to the REF sample (Figure 3b), implying lower recombination of photogenerated carriers in the K_2S absorber bulk.[33] The K_2S device displays comparatively lower EQE response in the long wavelength range due to the degradation

of long wavelength absorption owing to high S content in the absorber.[34] Figure S10 shows the corresponding band gaps of 1.148 and 1.189 eV for the REF and K_2S devices. For CZTSSe devices, V_{OC} usually increases with increasing band-gap, which coincides with the higher V_{OC} of K_2S devices. The EQE decays exponentially in the long wavelength range, while the Urbach energy (E_U) is one of the parameters describing the extent of the band-tail state that leads to such a decay. Thus, we also analyzed the Urbach energy of both the devices (Figure 3c).[4] E_U values reduced from 35.7 meV (REF) to 30.5 meV (K_2S), indicating the decreasing tailing state of the K_2S absorber and reducing the $V_{OC\text{-}def}$. The presence of intrinsic deep defects as recombination centers or band tails contributing to Shockley-Read-Hall recombination limits the useful energy of photogenerated carriers and their transport.[3, 31] Typically for kesterite material, the band-tailed state is caused by two known fundamental mechanisms: a high concentration of deep defects with a high degree of compensation, leading to electrostatic potential fluctuation; or inhomogeneity in the crystalline or composition, leading to band and band gap fluctuations. The band-gap fluctuation (σ_g) and the electrostatic potential fluctuation (γ_{opt}) can be extracted by redrawing EQE as a function of energy in the long wavelength range according to literature (Figure 3d, e).[35, 36] The σ_g were 142 meV for the REF device and 101 meV for K_2S device. The potential fluctuations in polycrystalline CZTSSe materials usually act as potential traps for carriers, which is a key factor limiting the carrier transport/diffusion performance in the devices. The formation of charged defects (for example $[Cu_{Zn}^{-}+Zn_{Cu}^{+}]$ is the most abundant because it has the lowest formation energy) and the magnitude of the

dielectric constant are the main factors that determine the fluctuation of electrostatic potential.[9, 37] The γ_{opt} of the REF and K_2S devices are 34.2 meV and 28.4 meV, respectively, indicating that K_2S devices have fewer defect complexes, which may be related to the reduction of $[Cu_{Zn}^{-}+Zn_{Cu}^{+}]$ due to the substitution of K^+ for Cu^+. Transient photovoltage decay (TPV) measurements were used to investigate the carrier recombination dynamics in CZTSSe devices.[22, 38] As shown in Figure 3f, the transient photovoltage decay lifetime (τ_{TPV}) of the REF device is 3.36×10^{-5} s, whereas the τ_{TPV} of the K_2S device is 8.19×10^{-5} s, indicating significantly suppressed nonradiative charge recombination in the K_2S device.

In order to clarify the elemental changes on the absorber surface of REF and K_2S device, XPS tests were performed. As shown in **Figure 4**a-c, the binding energy in the Cu 2p, Zn 2p and Sn 3d regions can be determined as Cu^+, Zn^{2+} and Sn^{4+}.[7] A shoulder peak located at 495.8 eV is observed near the Sn 3d3/2 peak of the REF film (Fig. 4c), which belongs to the Zn-Auger peak, possibly originate from Zn-based secondary phases or Zn-related defects. The peak does not appear in the K_2S film, implying that the K_2S layer suppresses the Zn related defects.[39] Four peaks were present in the S 2p spectrum (Fig. 4d, e), and the BE peaks at 160.9 and 162.1 eV belonged to S 2p, while the 159.6 eV and 165.3 eV belongs to the Se 3p core.[40, 41] Figure 4f, g shows the Se 3d XPS data for REF and K_2S films. Se-1 XPS peaks were observed in both samples (at 53.4 eV and 54.3 eV, respectively), which is assigned to the kesterite CZTSSe. For the K_2S film, it can be find an additional Se 3d contribution (Se-2) which is not assigned to CZTSSe at higher binding energy than Se-1.[42, 43] The peaks at lower binding energies of 52.8 eV

and 53.6 eV were assigned to the K_2Se_3 phase, confirming the presence of the K-Se phase.[44] Figure 4h, i shows the XPS spectra of the Se Auger-K 2p region. For the K_2S film, a shoulder peak on the Se Auger peak is observed at the low binding energy (292.6 and 249.8 eV) side, which is attributed to the K 2p response.[45]

The SEM data of REF film and K_2S film cross-sections in **Figure S11** revealed a dual layer of large grains on the top and fine grains at the bottom. This double-layer structure is commonly observed in solution progress CZTSSe absorbers.[46] The fine grain layer is caused by residual organic solvent impurity under selenization, which reduces the PCE. The crystallinity of K_2S sample is obviously improved and the fine grain layer is thinned. This is contrary to the usual conclusion that high S content deteriorates the crystallinity.[21, 22] To further investigate the effect of the K_2S layer on the grain growth mechanism, SEM analysis of REF samples and K_2S samples at different selenization stages (0 s/300 s/600 s/900 s) was carried out, as shown in **Figure 5**. Figures 5a-d and e-h show the surface and cross morphology of REF and K_2S samples at different selenization, respectively. As shown in Figure 5b and f, when the selenization time is 300 s, large grain appears on the surface and some fine grain formed at the back interface of REF sample; there are large grain on the surface and back interface of K_2S sample. When the selenization time was extended to 600s, the upper layer grain of REF sample increased significantly but the change of fine grain at the back interface was not obvious (Figure 5c). However, the upper and lower grain of K_2S sample increased visibly and the two layers were in contact with each other (Figure 5g). When the selenization time was further extended to 900 s, the size of the upper large grain of REF

sample increased and formed a typical double layer structure, while two large grain layers of K_2S sample fused with each other and further grew into single large grain. The above results confirm that the grain growth rate of the K_2S film is faster than REF film with the same selenization time, and the K_2S led to enhance the grain size and improve the CZTSSe crystallization. The significant improvement in grain growth rate is attributed to the formation of K-Se phase during selenization.[22] The band-gap fluctuation and electrostatic potential fluctuation were slightly higher for REF than for K_2S, which is consistent with the relatively good homogeneity due to the grain growth mechanism of the K-Se liquid phase.

During the selenization of CZTSSe, the diffusion of K atoms in CZTSSe films consists of two ways: the first one is the movement of K atoms through vacancy defects,[9]

$2V_{Cu}+K_2S\ (s) \rightarrow 2K_{Cu}+S\ (g)$

Several theoretical calculations have demonstrated that K_{Cu} does not form as easily thermodynamically as Na_{Cu}.[9] Therefore K atoms prefer the second type of diffusion: diffusion through gaps, voids and particles in CZTSSe films. The high affinity energy of K for Se at high temperatures and with an adequate supply of selenium vapor leads to the formation of a series of K-Se phases generated,[47]

$K_2S+5Se \rightarrow K_2Se_5+S$ (Starting temperature: 195 ℃)

$K_2S+2Se \rightarrow 2KSe_2+S$ (Starting temperature: 206 ℃)

$K_2S+3Se \rightarrow K_2Se_3+S$ (Starting temperature: 375 ℃)

In Figure 4g, the peaks located at higher affinity energy (52.8 eV and 53.6 eV) belong to the K_2Se_3 phase, confirming the presence of the K-Se phase. After the selenization

temperature reaches 375 ℃, the liquid K_2Se_3 phase flows between grain boundary (Figure 5i), lowering the melting point and leading to rapid crystallization at lower temperatures.[44] Moreover, the flow of K_2Se_3 liquid phase is accompanied by the supply of Se. Placing the K_2S layer in the middle of the CZTSSe film facilitates the downward diffusion of the generated K_2Se_3 to the rest of the film, which is the key reason why the film is able to form two layers of microcrystals when selenization time is 600 s. Meanwhile, the Cu_2Se liquid phase also plays an obvious role in accelerating the crystallization process, and Cu_2Se is usually formed in the pre-selenization period,

$Cu_2S+Se \rightarrow Cu_2Se+S$ (g)

this reaction occurs at 275 ℃, but the presence of the Cu_2Se phase can be detected at 225 ℃ when film containing alkali metals, so we believe that this is another reason for the dominance of the K_2S sample in the grain growth process.[48] In addition, K_2S readily reactivates with Sn to form wide band-gap alkali metal compound ($K_2Sn_2S_5$) as follow,[49]

$K_2S+Sn+S \rightarrow K_2Sn_2S_5$ (Starting temperature: 275 ℃)

The Sn in this reaction comes from the formation and decomposition of $SnSe_2$,[31]

$SnS+Se_2 \rightarrow SnSe_2+S$

$SnSe_2 \rightleftharpoons SnSe+Se$ (g) (Starting temperature: 340 ℃)

$3SnSe \rightleftharpoons 2Sn+SnSe_3$ (Starting temperature: above 400 ℃)

Theoretical calculations show that the formation energy of $K_2Sn_2S_5$ is very low (-7.36 eV) during the formation of K-doped kesterite.[50] This wide band-gap alkali compound has a substantially smaller VBM because the alkali metal atoms lack the 3d orbital

necessary to hybridize with the S 3p orbital. As a result, it can introduce hole barriers at grain boundaries and surfaces to prevent electron-hole recombination.[50] This property reflects the specificity and superiority of the choice of K_2S material to treat the absorber.

PL spectroscopy is a powerful optical method to characterize solar cells. PL emission of CZTSSe involving tail-state transition usually presents asymmetric PL bands. **Figure S12** shows the normalized photoluminescence spectra of REF and K_2S films. The difference between the PL peak and band-gap is larger is mainly due to band tailing caused by γ_{opt}, associated with the $V_{OC\text{-}def}$. The PL peaks are shifted toward lower energy relative to $E_{g,EQE}$, using the value of $E_{g,EQE}$-$E_{g,PL}$ to characterize the energy band fluctuation.[31] **Table 2** shows the $E_{g,EQE}$-$E_{g,PL}$ difference for REF and K_2S films. Due to the different band gap, the difference is 103 meV for the K_2S film, which is smaller than that of the REF film (129 meV). It means that the defects in K_2S film are reduced and the potential fluctuations are suppressed, which is beneficial to reduce the $V_{OC\text{-}def}$.[51] The Gaussian fit to the PL curves shows that both the main peak (peak 1) and the secondary peaks (peaks 2 and 3) are present (**Figure 6**). According to theoretical calculations, the formation energy of V_{Cu} (20-50 meV) and Cu_{Zn} (120-200 meV) are lower than the other acceptor and donor defects which leads to the electrons and holes recombination in the conduction and valance band respectively. Thus, the CZTSSe films also exhibit an inherent p-type conductivity.[37] Figure 6b and d shows a schematic diagram of the band electron structure. P1 (1.021 eV, REF film) and P1* (1.063 eV, K_2S film) are assigned as FB1 (FB stands for free carrier-band transition), involving the

most abundant shallow defect Cu_{Zn} in CZTSSe. P2 (1.127 eV) and P2* (1.159 eV) are again matched with the FB transition, assigned as FB2, involving valence band and V_{Cu} vacancy site defects. This can also be considered as band-band (BB) transitions due to their small difference from the CZTSSe band-gap, indicating recombination of the free electrons in the conduction band with the holes in the E_V.[37] The P3 peak of the REF film (0.944 eV) is assigned as FB3 with respect to V_{Sn}. An interesting difference in the PL spectra of the two samples is the almost complete quenching of P3* in the K_2S film, leaving P1* and P2*. This PL shows that K_2S can effectively passivate the acceptor defect (V_{Sn}), and it has been demonstrated that K is able to reduce Sn-related defects by promoting elemental diffusion to stabilize the Sn content.[52] Therefore, the supply of K_2S modified the defect chemistry of CZTSSe by reducing the transition path passing through the defects and passivating the non-radiative defects in CZTSSe. In multi-crystalline CIGS and CZTSSe materials, potential fluctuation usually can act as traps for carriers to hinder carrier transport and diffusion. The non-uniformity of electrons and the energy depth of potential fluctuations are the key factors limiting the carrier transport/diffusion properties, the superposition of σ_g and γ_{opt} is able to describe any spatial variation in the E_C and E_V. Both fluctuations occur simultaneously in the actual absorber, leading to a total variation width $\sigma_{total}=\sqrt{{\sigma_g}^2+{\gamma_{opt}}^2}$, with $\sigma_{total,\ K_2S}$ (104 meV) reduced by 1/3 compared to $\sigma_{total,\ REF}$ (146 meV).

To further investigate the carrier density and collection characteristic of the CZTSSe absorber, the *C-V* profile and the DLCP are shown in **Figure 7**a. The free carrier concentration of the K_2S devices (3.19×10^{15} cm^{-3}) is slightly increased compared to the

REF devices (3.01×10^{15} cm^{-3}).K cannot form Li_{Zn} defects to provide additional carriers like Li, however the formation of antisite defects is not the only influencing factor when considering the carrier concentration in the K-doped devices. Instead, grain size also plays a crucial role. As shown in Figure 5, the grain size of K_2S films is significantly larger than that of REF films. Larger grain size indicates fewer grain boundaries, which mitigates non-radiative recombination and increases carrier density. The W_d of the REF device and the K_2S device are 0.197 μm and 0.203 μm, respectively. In general, the larger W_d is more favorable for carrier collection and separation.[53, 54] The K_2S samples have better crystallinity and lower defect density, besides the superior carrier-carrier transport characteristics due to the double-gradient band-gap structure, which demonstrates better device performance. The DLCP allows more accurate assessment of the free carriers and deep defect states than *C-V* measurement, while the *C-V* also include the effect of the interface state in kesterite-based cells. Thus the contribution of the interface state can be extracted by subtracting the DLCP result from the *C-V* result.[11, 31] The reduction in N_{CV}-N_{DL} (zero bias) imply a reduction in interface traps. The K_2S device, by virtue of its low interface defect density (5.60×10^{14} cm^{-3} for the K_2S device and 9.06×10^{14} cm^{-3} for the REF device), makes interface recombination easier to control. In addition, the defects cannot respond effectively at high frequency, only free carriers contribute to the DLCP signal at high frequency. In contrast, the low-frequency capacitance represents the response of the total of free carriers and deep traps, which means that the DLCP is able to observe the response of free carriers and deep defects at low frequency. Therefore, the difference between the high and low frequency

DLCP responses is mainly related to the bulk defect density.[43] The bulk defect density of REF device and K_2S device is 1.31×10^{15} and 6.80×10^{14} cm^{-3}, respectively. Normally CZTSSe devices with high S content exhibit higher bulk defect density while K_2S device with higher sulfur content but lower bulk defect density is attributed to the existence of alkali metal K which plays a major role in passivating the defects.[34, 52] The minority carrier diffusion length (L_d) is one of the important parameters affecting the collection efficiency, bias-dependent EQE (**Figure S13**), reflectivity (**Figure S14**) and *C-V* measurements (**Figure S15**) were performed to investigate the L_d of REF and K_2S device.[55] The REF device has a strong W_d dependence (large slope) and the L_d value obtained is 0.77 μm. The derived L_d value is estimated from Figure 7e to be about 1.38 μm for K_2S devices with a small W_d dependence (small slope). Since the extracted L_d value exceeds the thickness of the sample, the true L_d is expected to be larger than the thickness of the absorber (1.2 μm).[55] In fact, this phenomenon has been observed in high performance CIGS solar cells, and it is hypothesized that the generation of L_d values larger than the absorber thickness is related to the back surface field.[55] For K_2S devices, the back gradient can provide a stronger back surface field to drive electron transport to the p-n junction compared to REF devices, thus increasing the minority carrier diffusion length and facilitating the reduction of back interface recombination. The optimization of the band-tailed state can also effectively improve the L_d. In addition, the carrier mobility is calculated from the equation $L_d = \sqrt{\mu_e k_b T/q}$ (where k_b is Boltzmann constant, T is temperature, and q is the elementary charge).[55] The electron mobility (μ_e) of REF and K_2S devices are 23 and 74 $cm^2\ V^{-1}s^{-1}$, respectively. The large

grains of the K_2S absorber reduces grain boundary scattering, which is more favorable for minority carrier diffusion. Also, the band-gap fluctuation caused by charge compensation can lead to small mobility, and the smaller band-gap fluctuations and electrostatic potential fluctuations of K_2S device are favorable for carrier mobility.[56] The defect property of semiconductor materials largely determines the transport characteristics of photogenerated carriers, which in turn affects the performance parameters of photovoltaic devices. Therefore the longer L_d means the shallower defect energy level and the smaller defect density. Defect formation is highly dependent on the reaction process, crystallinity and absorber composition. To further evaluate the defect energy level and defect density of REF device and K_2S device, the property of defects was investigated using DLTS. Figure 7f shows the DLTS signal in the temperature range of 120-350 K. It can be seen that two negative peaks (H1 and H2) appear in both samples, indicating the detection of two defects, the negative peak being assigned to the acceptor defect in the kesterite film. One (peak 1) is close to 220 K and the other (peak 2) is close to 270 K, indicating similar defect characteristics for both absorbers. The defect activation energy (E_a), defect density (N_T), and capture cross section (σ) of the defects can be extracted from the Arrhenius plot (Figure 7g) and summarized in **Table 3**.[4, 22] The defects of both devices have similar E_a, which means that they have similar origins. Among them, defects H1 and H2 are located 0.27-0.29 and 0.30-0.33 eV above the E_V, and combined with theoretical calculations, the H1 and H2 defects are identified as V_{Sn} and Cu_{Sn} deep energy level accepter defects, respectively.[37] In deep trap centers, a lower E_a value denotes a faster carrier emission.

H1 and H2 defects in the K_2S device have a lower activation energy than those in the REF device, decreasing their likelihood of functioning as efficient recombination centers. A schematic diagram in figure 7h and i clearly show the defect concentration and energy level of these defects. It is clear that both V_{Sn} and Cu_{Sn} are deep energy level defects and close to the middle of the band-gap, which are difficult to ionize at room temperature due to their high activation energy. Instead of affecting the doping type (n/p type) and carrier concentration, the deep defects typically operate as recombination centers, impairing carrier transit and lifetime. It is worth noting that the concentration of the V_{Sn} defect in K_2S device further reduced 6 times (from 3.79×10^{13} to 6.32×10^{12} cm^{-3}) compared to the REF device, confirming that the defects are sufficiently suppressed. The relatively small decrease in the Cu_{Sn} defect (2.3 times) compared to the sharp decrease in the V_{Sn} defect (6 times) is justified by the much higher formation energy of Cu_{Sn}. Agreeing with PL and DLCP results, the DLTS analysis demonstrates that K_2S devices have a lower defect density than REF devices. Considering that (E_g-qV_{OC}) is proportional to A$\ln N_T$ (where q is the elementary charge), lower N_T implies smaller V_{OC} deficit. Therefore, lower defect density in K_2S devices favors the open-circuit voltage, which is consistent with the *J-V* results.[57-59] Typically, sulfur-rich devices with higher defect density and deeper defect energy levels lead to stronger recombination, contrary to our conclusions.[34, 60] The decrease in the density of Sn-related deep defect states may be due to the existence of element K in the absorber layer of the K_2S device which enhances the element diffusion rate, allowing a larger fraction of the absorber to participate in the evaporation and inclusion during selenization,

stabilizing the Sn content.[52] This demonstrates the necessity of selecting K_2S material for CZTSSe, where the presence of K_2S is able to passivate deep energy level defects, thus reducing the defect problems that may result from the increased S content. Further calculations of $\sigma \times N_T$ to evaluate the trap lifetime are shown in figure 7j. It can be found that the two defects in the K_2S device have shorter lifetimes therefore the photo-generated holes and electrons are more likely to be trapped by the defects in the REF device, leading to severe trap-assisted recombination.

3. Conclusion

This work presents a simple and effective method for obtaining double gradient band-gap by inserting a K_2S layer into the CZTSSe precursor film to modulate the S/(S+Se) profile of the absorber for the first time. The PCE of champion CZTSSe devices based on the optimal double gradient band-gap structure is as high as 13.70%. EDS, SIMS, EQE and XPS results clearly demonstrate the formation of an ideal double gradient band-gap gradient in CZTSSe solar cell. It is shown that K_2S provided additional S to the absorber and the high affinity of K-Se optimized the Se profile and makes the K_2S layer locally Se rich and S poor during selenization. It means that during the high temperature selenization process, the S and Se distribution in the absorber was adjusted and the S/(S+Se) notch appeared at the location of K_2S layer, implying that the band-gap was distributed in similar double gradient. In addition, the K-Se liquid phase (K_2Se_3) formed during selenization contributes to lowering of the melting point to promote grain growth, which helps to increase the minority carrier diffusion length. At the same

time, the presence of K^+ stabilizes the Sn content by enhancing the elemental diffusion rate, thereby reducing the transition path through defects, passivating non-radiative defects and suppressing band-gap fluctuation and electrostatic potential fluctuation. The formation of wide band-gap alkali compound $K_2Sn_2S_5$ is conducive to enhancing the carrier separation ability at the grain boundary and reducing the electron-hole recombination. This method of obtaining a double-gradient band-gap absorber does not require additional equipment or change the structure of equipment, which makes it easy to introduced into the CZTSSe solar cells preparation progress with strong production applicability. These superior results and the associated discovery of material mechanisms may open up further opportunities and avenues for broadening the processing window of CZTSSe solar cells, thus further improving cell performance.

4. Experimental Section

Precursor preparation

The molar ratios of Cu/(Zn+Sn) and Zn/Sn in the CZTS precursor solution were 0.775 and 1.2, respectively. CuCl, $Zn(CH_3COO)_2 \cdot 2H_2O$, $SnCl_4 \cdot 5H_2O$, and $SC(NH_2)_2$ were dissolved into 2-methoxyethanol, and $Cu(CH_3COO)_2 \cdot H_2O$, $ZnCl_2$, $SnCl_2 \cdot 2H_2O$, $SC(NH_2)_2$ were dissolved into 2-methoxyethanol to obtain Sn^{4+} and Sn^{2+} precursor solutions, respectively. The precursor solutions containing Sn^{4+} and Sn^{2+} were homogeneously mixed 1:1 and diluted to half of the original concentration to obtain CZTS precursor solutions. K_2S solution was obtained by dissolving K_2S powder in ethanol. The concentration of K_2S solution was 0.01M, 0.05M and 0.1M, respectively.

Thin-film deposition

The CZTS precursor film was prepared by spin-coating progress. This process of Reference sample was repeated ten times to obtain a thickness of about 1.2 μm. K_2S samples were obtained by inserting K_2S layers at different locations in the CZTSSe precursor films: 0L-K_2S samples were obtained by spin-coating the K_2S solution on the Mo substrate followed by 10 layers of CZTSSe solution. 10L-K_2S samples were obtained by spin coating 10 layers of CZTSSe solution followed by K_2S solution. 3L-K_2S and 6L-K_2S samples were obtained by inserting K_2S layers after spin-coating 3 and 6 layers of CZTSSe precursor solution, respectively. The same spin-coating parameters were used for the CTZS film and the K_2S layer. The solution was spin-coated with 3000 rpm for 20 s, and the wet film was immediately annealed at 280 ℃ for 2 min on a hot plate.

Device fabrication

We utilize solid selenium particles as Se source and the selenium amount was 80 mg. The graphite box which contained the precursor film and selenium particles was placed in a rapid thermal processing furnace and heated from room temperature to 555 ℃ in 110 s and held for 15 min. After that, the RTP furnace was naturally cooled to room temperature. The selenization process was carried out under a flowing argon atmosphere. A CdS buffer layer about 60 nm thick was deposited on the surface of the CZTSSe absorber layer by chemical bath deposition. Then an approximately 200 nm thick ITO window layer was prepared using RF magnetron sputtering. Finally, silver electrodes were deposited on the top of the device using thermal evaporation.

Characterizations

Scanning electron microscopy (SEM) (SUPRA 55) was used to obtain microscopic images of the surface and cross-section of the absorber and energy dispersive spectroscopy (EDS) (BRUKER QUANTAX 200) was used to analyze the chemical composition of the samples. The *J-V* characteristics of the devices were measured under standard test conditions (100 mW cm^{-2}, 25 ℃, AM 1.5G) using a Keithley 2400 meter and a Zolix SS150 solar simulator. The external quantum efficiency (EQE) was measured using a Zolix solar cell QE/IPCE measurement system (solar cell Scan 100). The crystal structure of the CZTSSe films was characterized by x-ray diffraction (XRD, Ultima-iv). Ultraviolet Photoelectron Spectroscopy (UPS) was performed by PHI 5000 VersaProbe III with He I source (21.22 eV) under an applied negative bias of 9.0 V. X-ray photoelectron spectroscopy (XPS) was performed by PHI 5000 VersaProbe III with a monochromatic Al Kα X-ray source. The elemental depth composition curves were obtained by TOF SIMS 5 secondary ion mass spectrometry (SIMS) workstation (IONTOF GmbH). Transient surface photovoltage measurement was performed using a 355 nm pulsed laser (Quantel Brilliant Eazy, BRILEZ/IR-10) as the light source to excite the CZTSSe films and an oscilloscope (Tektronix TDS 3054C, 500 MHz) was used to record the voltage signal. A FluoTime 300 spectrometer with an excitation wavelength of 532 nm was used to measure photoluminescence (PL). Capacitance-voltage (*C-V*) analysis and driver-level capacitance analysis (DLCP) were performed using a Keithley 4200A-SCS system and a JANIS cryogenic platform. Reflection spectrum were analyzed using a UV-3600Plus UV-Vis Near Infrared Spectrophotometer (SHIMADZU). The deep level transient spectroscopy (DLTS) was obtained by the FT-1030 HERA DLTS system in configuration with a JANIS VPF-800 cryostat controller.

Acknowledgments

This work was supported by the National Natural Science Foundation of China (No. 62074102 and 62204067), Guangdong Basic and Applied Basic Research Foundation (2022A1515010979) China, Science and Technology plan project of Shenzhen (20220808165025003) China.

Conflict of Interest

The authors declare no conflict of interest.

Reference

[1] M. A. Green, E. D. Dunlop, M. Yoshita, N. Kopidakis, K. Bothe, G. Siefer and X. Hao, *Prog. Photovolt: Res. Appl.* **2023**, 31, 651-663.

[2] M. He, C. Yan, J. Li, M. P. Suryawanshi, J. Kim, M. A. Green and X. Hao, *Adv. Sci.* **2021**, 8, 2004313.

[3] X. Zhang, Z. Zhou, L. Cao, D. Kou, S. Yuan, Z. Zheng, G. Yang, Q. Tian, S. Wu and S. Liu, *Adv. Funct. Mater.* **2022**, 33, 2211315.

[4] Y. Gong, R. Qiu, C. Niu, J. Fu, E. Jedlicka, R. Giridharagopal, Q. Zhu, Y. Zhou, W. Yan, S. Yu, J. Jiang, S. Wu, D. S. Ginger, W. Huang and H. Xin, *Adv. Funct. Mater.* **2021**, 31, 2101927.

[5] S. Jung, S. Ahn, J. H. Yun, J. Gwak, D. Kim and K. Yoon, *Curr. Appl. Phys.* **2010**, 10, 990-996.

[6] M. Ochoa, S. Buecheler, A. N. Tiwari and R. Carron, *Energy Environ. Sci.* **2020**, 13, 2047-2055.

[7] Y. Du, Q. Tian, J. Huang, Y. Zhao, X. Chang, A. Zhang and S. Wu, *Sustainable*

Energy Fuels **2020**, 4, 1621-1629.

[8] Y. Du, S. Wang, Q. Tian, Y. Zhao, X. Chang, H. Xiao, Y. Deng, S. Chen, S. Wu and S. Liu, *Adv. Funct. Mater.* **2021**, 31, 2010325.

[9] Z.-K. Yuan, S. Chen, Y. Xie, J.-S. Park, H. Xiang, X.-G. Gong and S.-H. Wei, *Adv. Energy Mater.* **2016**, 6, 1601191.

[10] X. Zhao, X. Chang, D. Kou, W. Zhou, Z. Zhou, Q. Tian, S. Yuan, Y. Qi and S. Wu, *J. Energy Chem.* **2020**, 50, 9-15.

[11] J. Zhou, X. Xu, B. Duan, H. Wu, J. Shi, Y. Luo, D. Li and Q. Meng, *Nano Energy* **2021**, 89, 106405.

[12] E. Avancini, R. Carron, B. Bissig, P. Reinhard, R. Menozzi, G. Sozzi, S. Di Napoli, T. Feurer, S. Nishiwaki, S. Buecheler and A. N. Tiwari, *Prog. Photovolt: Res. Appl.* **2017**, 25, 233-241.

[13] T. Kato, *Jpn. J. Appl. Phys.* **2017**, 56, 04CA02.

[14] Q. Fan, Q. Tian, H. Wang, F. Zhao, J. Kong and S. Wu, *J. Mater. Chem. A* **2018**, 6, 4095-4101.

[15] A. Chirila, S. Buecheler, F. Pianezzi, P. Bloesch, C. Gretener, A. R. Uhl, C. Fella, L. Kranz, J. Perrenoud, S. Seyrling, R. Verma, S. Nishiwaki, Y. E. Romanyuk, G. Bilger and A. N. Tiwari, *Nature materials* **2011**, *10*, 857-861.

[16] Y.-F. Qi, D.-X. Kou, W.-H. Zhou, Z.-J. Zhou, Q.-W. Tian, Y.-N. Meng, X.-S. Liu, Z.-L. Du and S.-X. Wu, *Energy Environ. Sci.* **2017**, *10*, 2401-2410.

[17] H. Guo, R. Meng, G. Wang, S. Wang, L. Wu, J. Li, Z. Wang, J. Dong, X. Hao and Y. Zhang, *Energy Environ. Sci.* **2022**, *15*, 693-704.

[18] M. Kauk-Kuusik, X. Li, M. Pilvet, K. Timmo, V. Mikli, R. Kaupmees, M. Danilson and M. Grossberg, *J. Mater. Chem. A* **2019**, *7*, 24884-24890.

[19] J. Márquez, H. Stange, C. J. Hages, N. Schaefer, S. Levcenko, S. Giraldo, E. Saucedo, K. Schwarzburg, D. Abou-Ras, A. Redinger, M. Klaus, C. Genzel, T. Unold and R. Mainz, *Chem. Mater.* **2017**, *29*, 9399-9406.

[20] Z. Zhang, Y. Qi, W. Zhao, J. Liu, X. Liu, K. Cheng and Z. Du, *J. Alloys Compd.* **2022**, *910*, 164665.

[21] J. H. Kim, M. K. Kim, A. Gadisa, S. J. Stuard, M. M. Nahid, S. Kwon, S. Bae, B. Kim, G. S. Park, D. H. Won, D. K. Lee, D. W. Kim, T. J. Shin, Y. R. Do, J. Kim, W. J. Choi, H. Ade and B. K. Min, *Small* **2020**, *16*, e2003865.

[22] Y.-H. Zhao, Q.-Q. Gao, S.-J. Yuan, Q.-Q. Chang, T. Liang, Z.-H. Su, H.-L. Ma, S. Chen, G.-X. Liang, P. Fan, X.-H. Zhang and S.-X. Wu, *Chem. Eng. J.* **2022**, *436*, 135008.

[23] C. P. Muzzillo, *Sol. Energy Mater. Sol. Cells* **2017**, *172*, 18-24.

[24] A. R. Uhl, J. K. Katahara and H. W. Hillhouse, *Energy Environ. Sci.* **2016**, *9*, 130-134.

[25] T. Zhang, Y. Yang, D. Liu, S. C. Tse, W. Cao, Z. Feng, S. Chen and L. Qian, *Energy Environ. Sci.* **2016**, *9*, 3674-3681.

[26] U. Rau and H. W. Schock, *Appl. Phys. A* **1999**, *15*, 507-519.

[27] Thomas Feurer, Patrick Reinhard, Enrico Avancini, Benjamin Bissig, Johannes Löckinger, Peter Fuchs, Romain Carron, Thomas Paul Weiss, Julian Perrenoud, Stephan Stutterheim, Stephan Buecheler and A. N. Tiwari, *Prog. Photovolt: Res.*

Appl. **2017**, *25*, 645-667.

[28] M. Gloeckler and J. R. Sites, *J. Phys. Chem. Solids* **2005**, *66*, 1891-1894.

[29] A. Chirila, P. Reinhard, F. Pianezzi, P. Bloesch, A. R. Uhl, C. Fella, L. Kranz, D. Keller, C. Gretener, H. Hagendorfer, D. Jaeger, R. Erni, S. Nishiwaki, S. Buecheler and A. N. Tiwari, *Nature materials* **2013**, *12*, 1107-1111.

[30] Y. Gong, Q. Zhu, B. Li, S. Wang, B. Duan, L. Lou, C. Xiang, E. Jedlicka, R. Giridharagopal, Y. Zhou, Q. Dai, W. Yan, S. Chen, Q. Meng and H. Xin, *Nat. Energy* **2022**, *7*, 966-977.

[31] Z. Yu, C. Li, S. Chen, Z. Zheng, P. Fan, Y. Li, M. Tan, C. Yan, X. Zhang, Z. Su and G. Liang, *Adv. Energy Mater.* **2023**, *13*, 2300521.

[32] S. Kim, T. R. Rana, J. Kim, D.-H. Son, K.-J. Yang, J.-K. Kang and D.-H. Kim, *Nano Energy* **2018**, *45*, 75-83.

[33] Y. Zhao, S. Yuan, D. Kou, Z. Zhou, X. Wang, H. Xiao, Y. Deng, C. Cui, Q. Chang and S. Wu, *ACS Appl. Mater. Interfaces* **2020**, *12*, 12717-12726.

[34] H.-S. Duan, W. Yang, B. Bob, C.-J. Hsu, B. Lei and Y. Yang, *Adv. Funct. Mater.* **2013**, *23*, 1466-1471.

[35] S. Hadke, S. Levcenko, G. Sai Gautam, C. J. Hages, J. A. Márquez, V. Izquierdo-Roca, E. A. Carter, T. Unold and L. H. Wong, *Adv. Energy Mater.* **2019**, *9*, 1902509.

[36] Y. Gong, Y. Zhang, Q. Zhu, Y. Zhou, R. Qiu, C. Niu, W. Yan, W. Huang and H. Xin, *Energy Environ. Sci.* **2021**, *14*, 2369-2380.

[37] S. Chen, A. Walsh, X. G. Gong and S. H. Wei, *Adv. Mater.* **2013**, *25*, 1522-1539.

[38] B. Duan, L. Guo, Q. Yu, J. Shi, H. Wu, Y. Luo, D. Li, S. Wu, Z. Zheng and Q.

Meng, *J. Energy Chem.* **2020**, *40*, 196-203.

[39] Z. Tong, C. Yan, Z. Su, F. Zeng, J. Yang, Y. Li, L. Jiang, Y. Lai and F. Liu, *Appl. Phys. Lett.* **2014**, *105*, 223903.

[40] M. Danilson, M. Altosaar, M. Kauk, A. Katerski, J. Krustok and J. Raudoja, *Thin Solid Films* **2011**, *519*, 7407-7411.

[41] M. P. Suryawanshi, U. V. Ghorpade, U. P. Suryawanshi, M. He, J. Kim, M. G. Gang, P. S. Patil, A. V. Moholkar, J. H. Yun and J. H. Kim, *ACS omega* **2017**, *2*, 9211-9220.

[42] S. Harel, L. Arzel, T. Lepetit, P. Zabierowski and N. Barreau, *ACS Appl. Mater. Interfaces* **2020**, *12*, 46953-46962.

[43] E. Handick, P. Reinhard, J. H. Alsmeier, L. Kohler, F. Pianezzi, S. Krause, M. Gorgoi, E. Ikenaga, N. Koch, R. G. Wilks, S. Buecheler, A. N. Tiwari and M. Bar, *ACS Appl. Mater. Interfaces* **2015**, *7*, 27414-27420.

[44] M. Kim, G. D. Park and Y. C. Kang, *Int. J. Energy Res.* **2021**, *46*, 5800-5810.

[45] E. H. Alruqobah and R. Agrawal, *ACS Appl. Energy Mater.* **2020**, *3*, 4821-4830.

[46] Y. Zhao, Z. Yu, J. Hu, Z. Zheng, H. Ma, K. Sun, X. Hao, G. Liang, P. Fan, X. Zhang and Z. Su, *J. Energy Chem.* **2022**, *75*, 321-329.

[47] T. Maeda, A. Kawabata and T. Wada, *Phys. Status Solidi C* **2015**, *12*, 631-637.

[48] Y. Sun, S. Lin, W. Li, S. Cheng, Y. Zhang, Y. Liu and W. Liu, *Engineering* **2017**, *3*, 452-459.

[49] K. O. Klepp, *Z. Naturforsch.* **1992**, *47*, 197-200.

[50] X. Zhang, D. Han, S. Chen, C. Duan and J. Chu, *J. Energy Chem.* **2018**, *27*, 1140-

1150.

[51] H. Lee, Y. Jang, S. W. Nam, C. Jung, P. P. Choi, J. Gwak, J. H. Yun, K. Kim and B. Shin, *ACS Appl. Mater. Interfaces* **2019**, *11*, 35653-35660.

[52] S. Tao, L. Dong, J. Han, Y. Wang, Q. Gong, J. Wei, M. Zhao and D. Zhuang, *J. Mater. Chem. A* **2023**, *11*, 9085-9096.

[53] D. Wang, J. Wu, X. Liu, L. Wu, J. Ao, W. Liu, Y. Sun, Y. Zhang, *J. Energy Chem.* **2019**, *35*, 188.

[54] J. Guo, Y. Mao, J. Ao, Y. Han, C. Cao, F. Liu, J. Bi, S. Wang, Y. Zhang, *Small* **2022**, *18*, e2203354.

[55] T. Gokmen, O. Gunawan and D. B. Mitzi, *J. Appl. Phys.* **2013**, *114*, 114511.

[56] Y. Zhou, C. Xiang, Q. Dai, S. Xiang, R. Li, Y. Gong, Q. Zhu, W. Yan, W. Huang, H. Xin, *Adv. Energy Mater.* **2023**, *13*, 2300253.

[57] S. Wang, S. Gao, D. Wang, Z. Jiang, J. Ao, Z. Zhou, S. Liu, Y. Sun, Y. Zhang, *Solar RRL* **2019**, *3*, 1800236.

[58] Y. Sun, P. Qiu, W. Yu, J. Li, H. Guo, L. Wu, H. Luo, R. Meng, Y. Zhang, S. F. Liu, *Adv. Mater.* **2021**, *33*, e2104330.

[59] J. Guo, J. Ao, Y. Zhang, *J. Mater. Chem. A* **2023**, *11*, 16494.

[60] G. X. Liang, C. H. Li, J. Zhao, Y. Fu, Z. X. Yu, Z. H. Zheng, Z. H. Su, P. Fan, X. H. Zhang, J. T. Luo, L. Ding, S. Chen, *SusMat* **2023**, DOI: 10.1002/sus2.160.

Table 1 The comparison of photovoltaic parameters of sample A-M.

	REF	0.01	0.01	0.01	0.01	0.05	0.05	0.05	0.05	0.1	0.1	0.1	0.1
Layer	-	0L	3L	6L	10L	0L	3L	6L	10L	0L	3L	6L	10L
Device	A	B	C	D	E	F	G	H	I	J	K	L	M
J_{SC} (mA/cm^2)	35.19	36.43	36.31	36.37	36.44	36.61	36.49	36.73	36.38	36.03	36.65	36.42	36.51
V_{OC} (mV)	0.512	0.519	0.525	0.532	0.511	0.543	0.526	0.544	0.524	0.527	0.523	0.529	0.519
FF (%)	62.27	61.78	64.64	68.30	63.23	63.33	65.40	68.48	64.14	61.67	63.85	65.34	63.53
PCE (%)	11.23	11.68	12.33	13.20	11.76	12.58	12.57	13.70	12.23	11.72	12.24	12.60	12.06

Table 2 Summary of result derived from EQE, PL and TPV.

	$E_{g,EQE}$ (eV)	E_U (meV)	σ_g (meV)	γ_{opt} (meV)	$E_{g,PL}$ (eV)	$E_{g,EQE}$-$E_{g,PL}$(meV)	σ_{total} (meV)	τ_{TPV} (s)
REF	1.148	35.7	142	34.2	1.019	129	146	3.36×10^{-5}
K_2S	1.189	30.5	101	28.4	1.086	103	104	8.19×10^{-5}

Table 3 Summary of result derived from DLTS.

	Peak ID	E_a (eV)	N_T (cm^{-3})	σ (cm^2)	$\sigma\times N_T$	Possible defect level
REF	H1	0.287	3.79×10^{13}	6.92×10^{-18}	2.62×10^{-4}	V_{Sn}
	H2	0.327	3.97×10^{14}	3.46×10^{-18}	1.37×10^{-3}	Cu_{Sn}
K_2S	H1	0.270	6.32×10^{12}	4.72×10^{-18}	2.98×10^{-5}	V_{Sn}
	H2	0.305	1.68×10^{14}	1.57×10^{-18}	2.64×10^{-4}	Cu_{Sn}

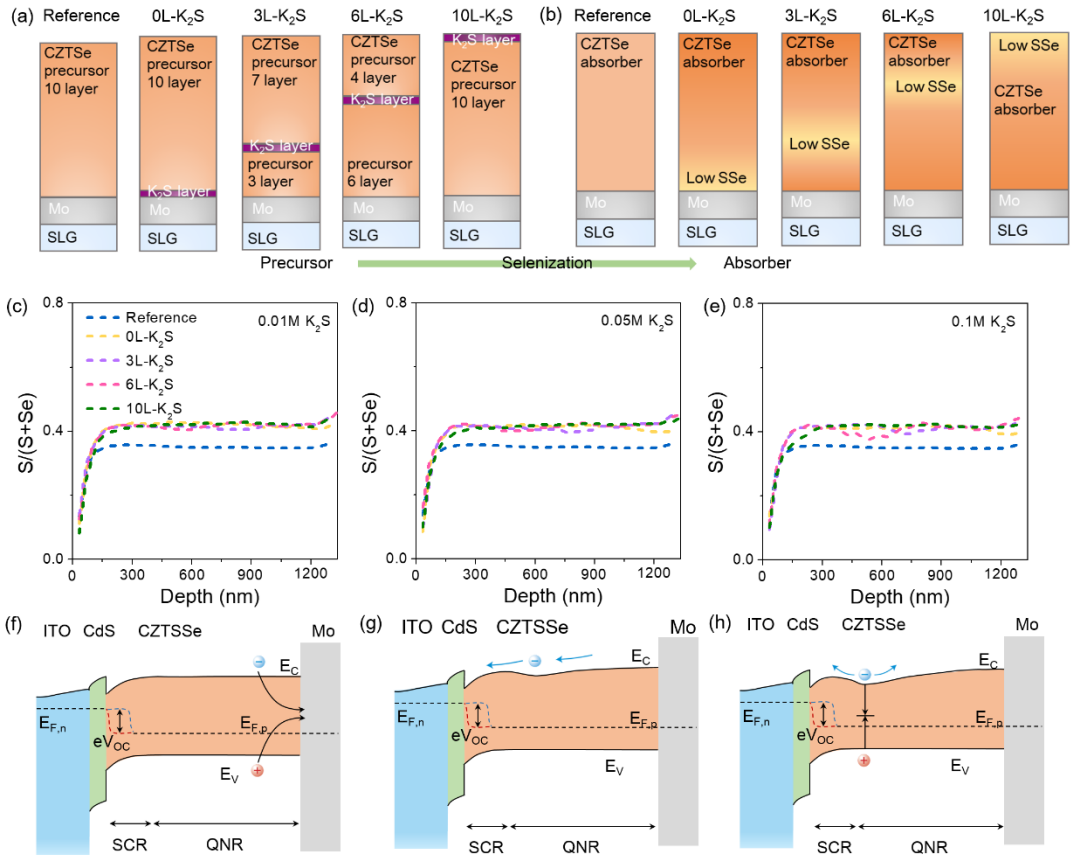

Figure 1 (a) Experimental schematic diagram of reference precursor and K_2S precursor, K_2S layer is denoted as a purple layer. (b) Schematic distribution of S/(S+Se) after selenization of the reference absorber and K_2S absorber. (c-e) S/(S+Se) atomic concentration depth profiles of the Reference (blue), 0L-K_2S (yellow), 3L-K_2S (violet), 6L-K_2S (pink) and 10L-K_2S (green) films detected by EDS, the concentration of K_2S solution is 0.01 M (c), 0.05 M (d) and 0.1 M (e). (f) The band diagram of CZTSSe solar cell. (g) Schematic band diagram of an optimized grading profile. (h) Schematic band diagrams of too pronounced grading profile.

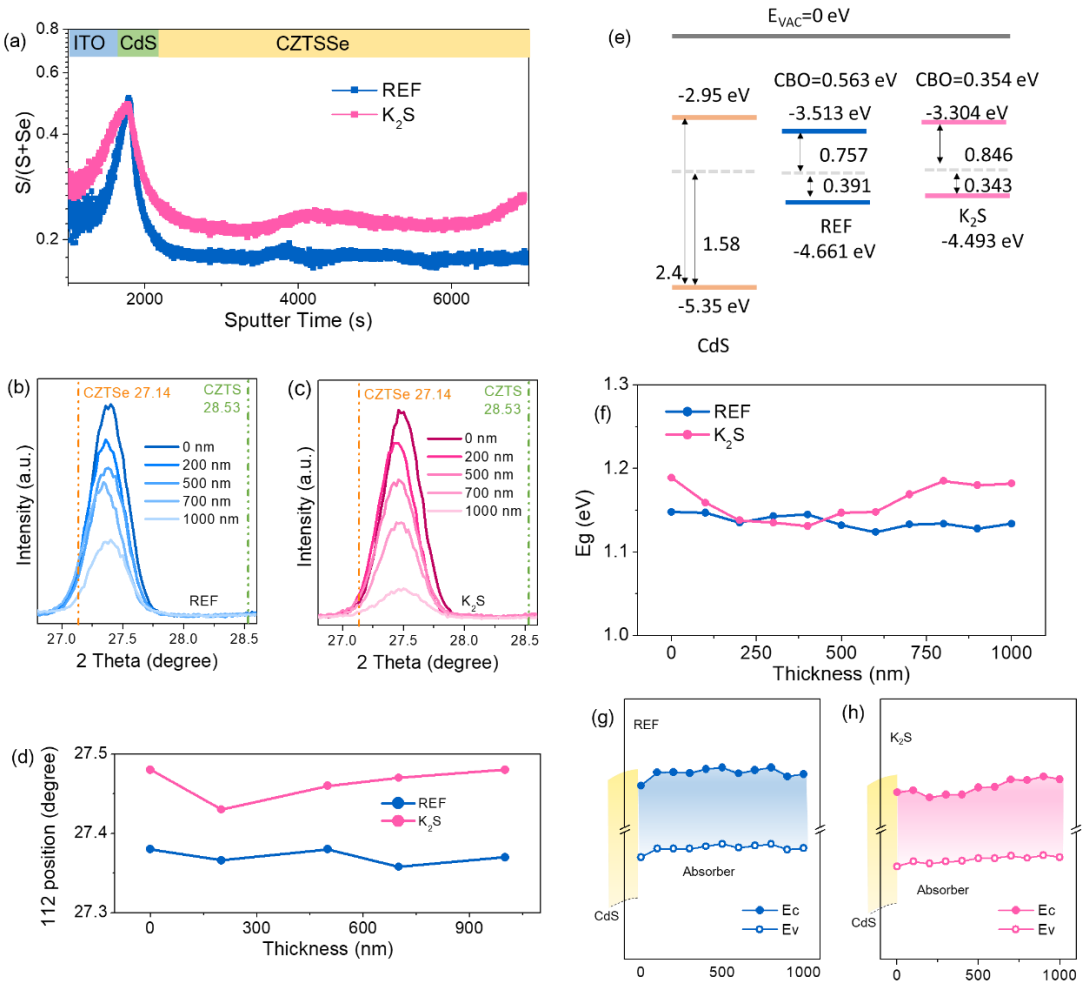

Figure 2 (a) S/(S+Se) depth profile of the REF and K_2S device along the CZTSSe film depth as assessed by SIMS measurements. The enlarged view of XRD patterns (112) peak of etched REF (b) and K_2S (c) films. (d) The position of (112) crystal plane. (e) Band alignment of valence and conduction bands between absorber and CdS of REF and K_2S sample. (f) Band-gap depth profile of the REF and K_2S device along the CZTSSe film depth as assessed by EQE measurements. Valence and conduction bands depth profile of the REF (g) and K_2S (h) device along the CZTSSe film depth.

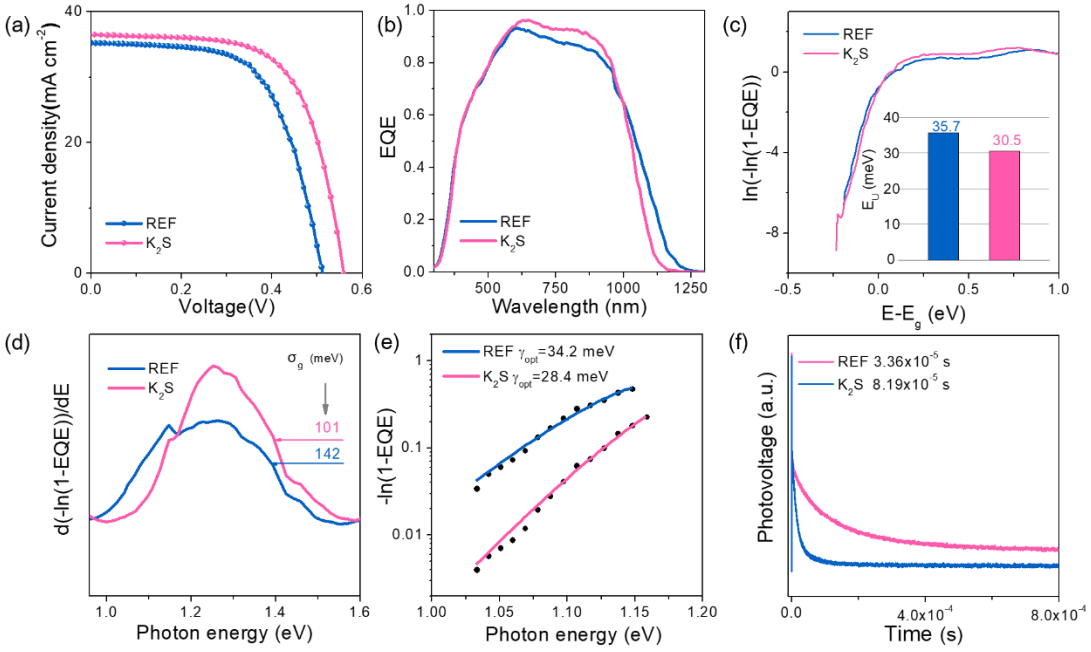

Figure 3 (a) *J*−*V* curves of the reference and champion device. (b) EQE curves of reference and champion device. (c) Calculated Urbach energy. (d) The extraction of band-gap fluctuation. (e) The extraction of electrostatic potential fluctuation. (f) TPV spectra of reference and champion device.

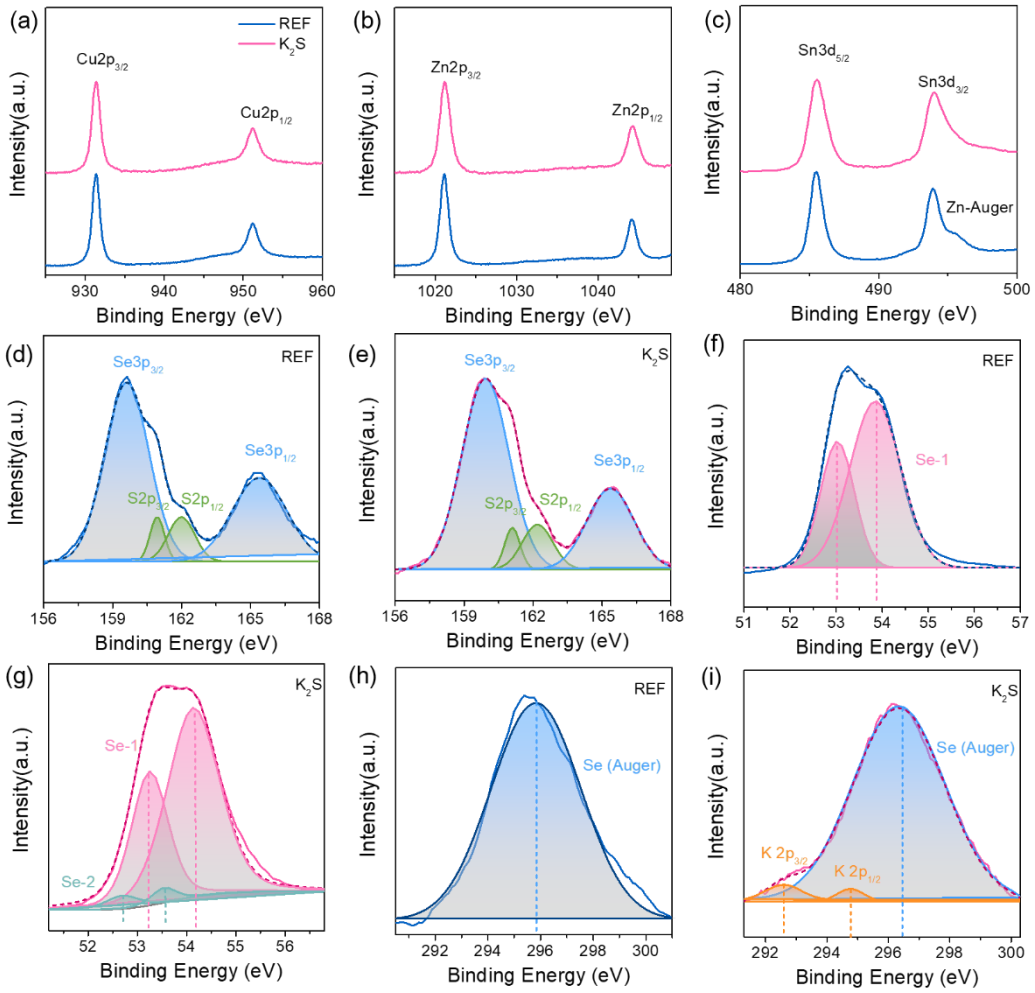

Figure 4 The (a) Cu 2p, (b) Zn 2p, (c) Sn 3d XPS spectra of the REF and K_2S films; (d, e) S2p and (f, g) Se 3d XPS spectra of the REF and K_2S films; (h, i) K 2p photoelectron transitions of REF and K_2S films.

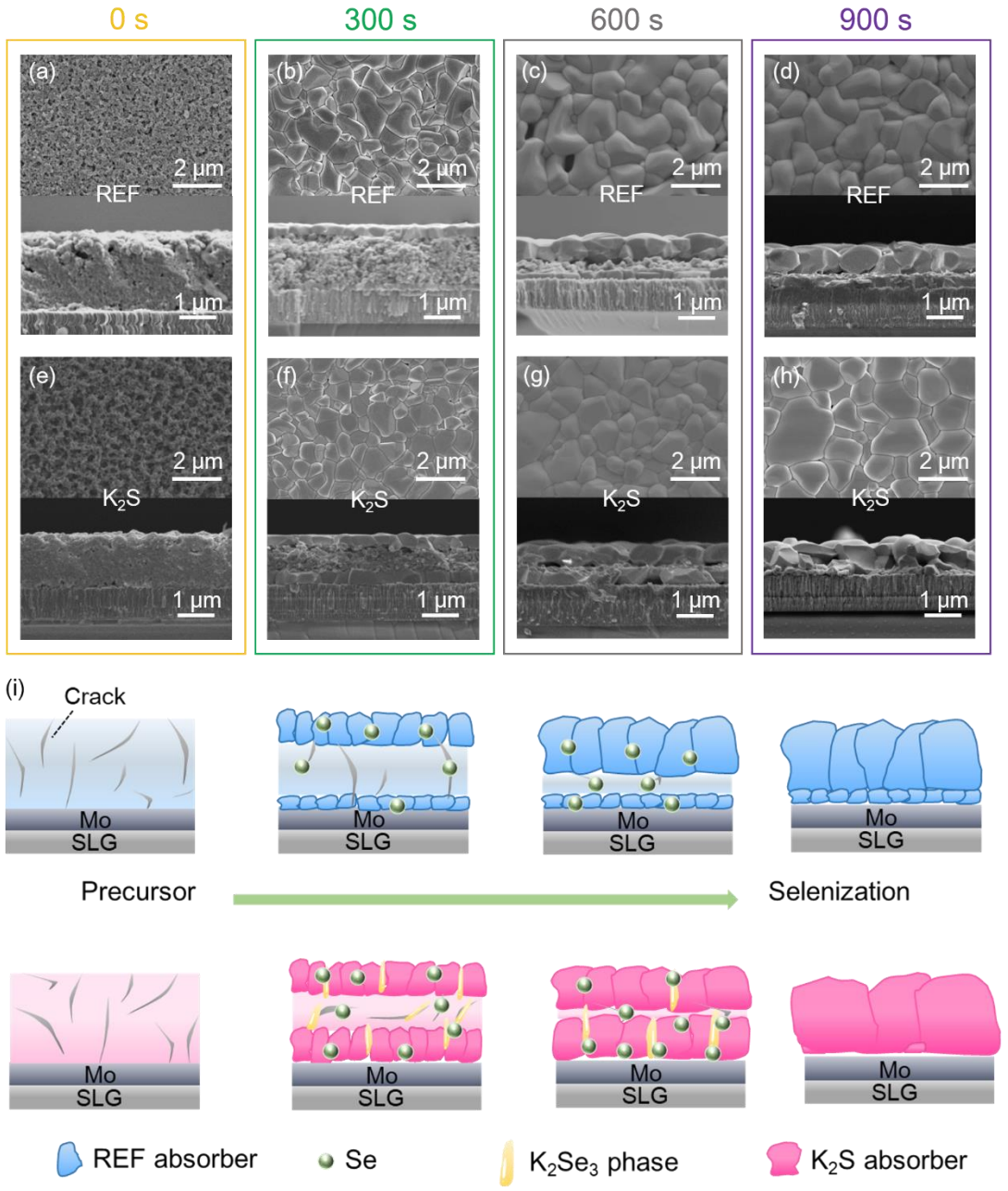

Figure 5 Top and cross SEM images of (a)-(d) REF and (e)-(h) K_2S films at the selenization process of 0, 300, 600, and 900s. (i) Schematic illustration of growth mechanism for the REF and K_2S film during selenization process.

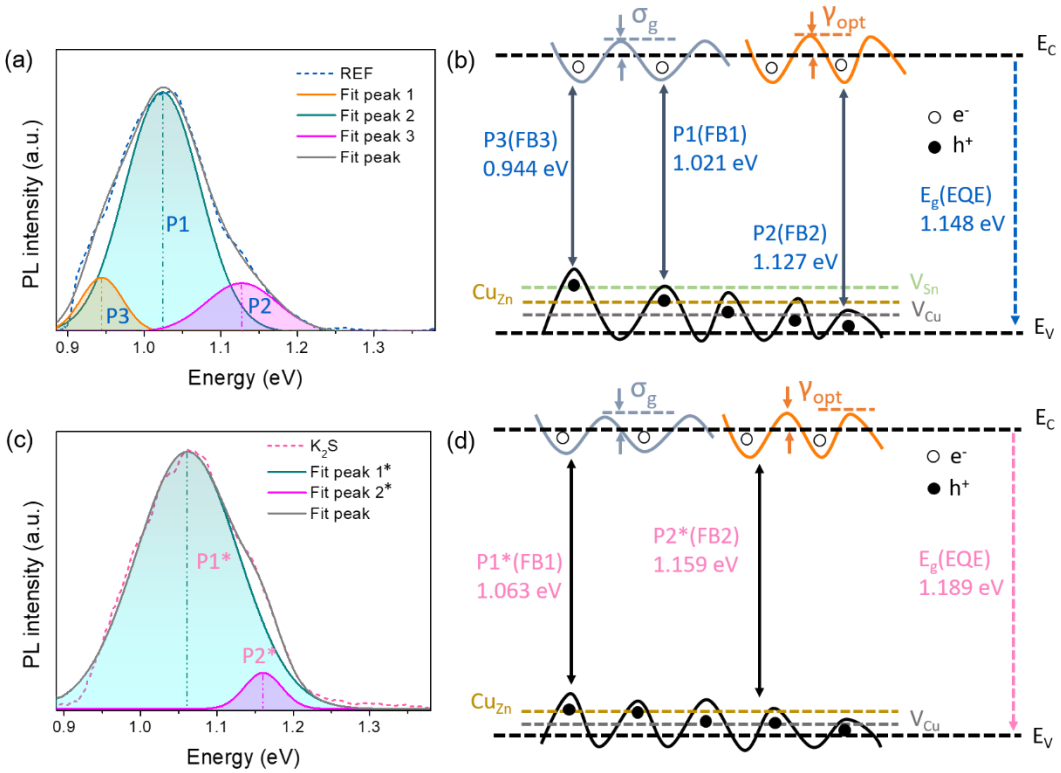

Figure 6 The peak-differenating analysis of the PL spectrum of (a) REF film and (c) K_2S film. Schematics of transitions for each peak designated of (b) REF film and (d) K_2S film including band-gap and electrostatic potential fluctuations.

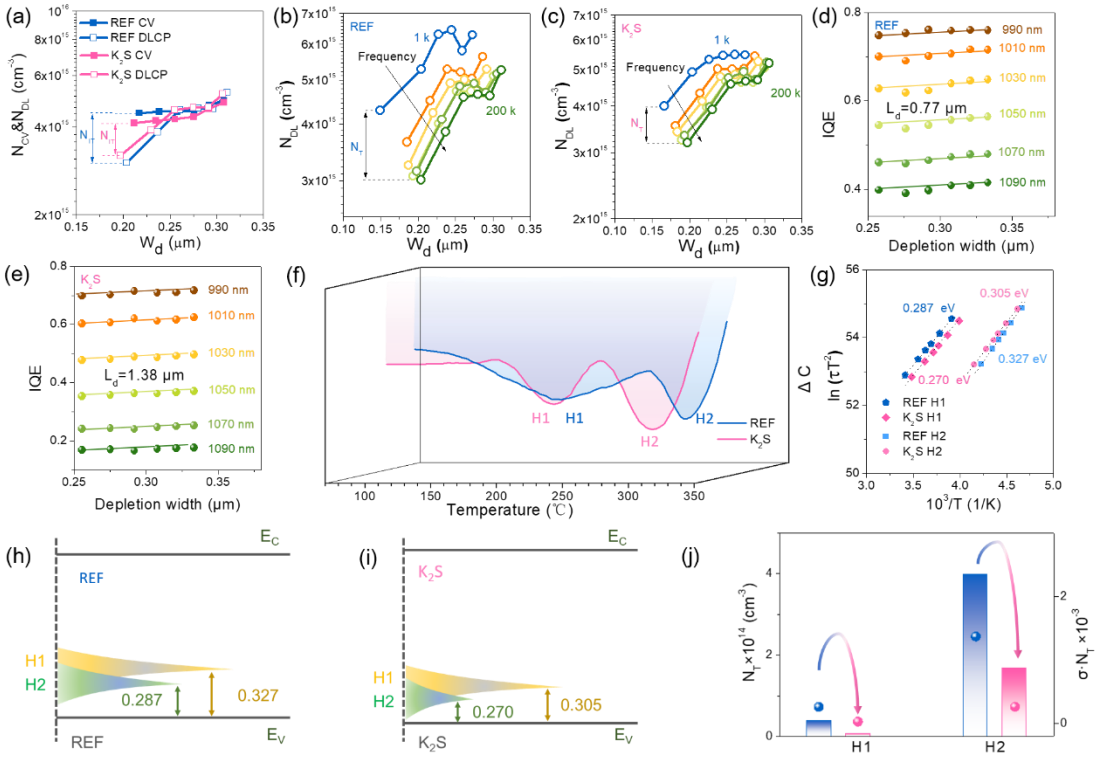

Figure 7 (a) The *C*–*V* and DLCP profiles of REF and K_2S device. N_{DL} of (b) REF device and (c) K_2S device measured at frequencies from 1 to 200 kHz. Minority carrier diffusion length extraction of (d) REF device and (e) K_2S device. (f) C-DLTS spectra of REF and K_2S samples and (g) the corresponding Arrhenius curves. The schematic diagram of E_a and N_T of (h) REF device and (i) K_2S device. (j) The values of N_T and ($\sigma \cdot N_T$) at H1 (Cu_{Sn}) and H2 (V_{Sn}) defects.

Title: Controllable Double Gradient Band-gap Strategy Enables High Efficiency Solution-Processed Kesterite Solar Cells

Table of contents: The controllable preparation of double gradient band-gap structure was realized by spin-coating K_2S solution during the preparation of precursor films to obtain high-efficiency CZTSSe devices with high crystalline quality and low defect density.

ToC Figure

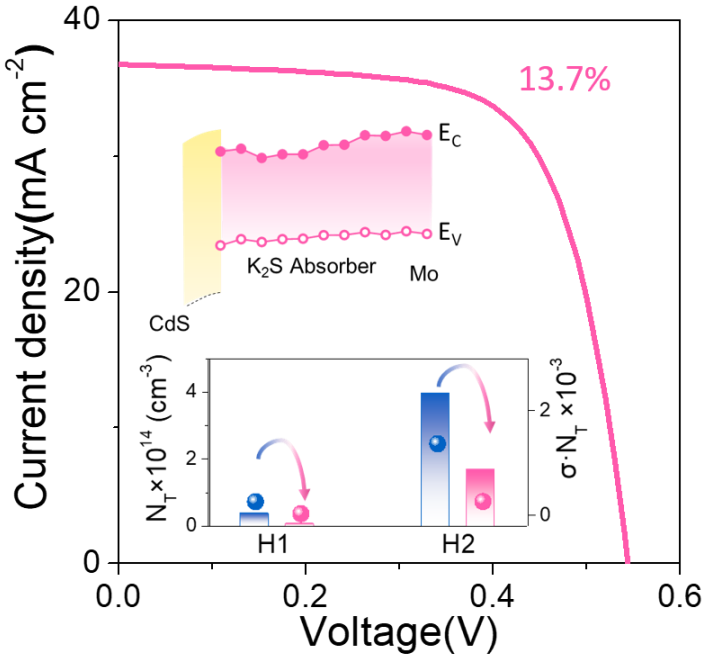

Supporting Information

Controllable Double Gradient Band-gap Strategy Enables High Efficiency Solution-Processed Kesterite Solar Cells

Yunhai Zhao, Shuo Chen, Muhammad Ishaq, Michel Cathelinaud, Chang Yan, Hongli Ma, Ping Fan, Xianghua Zhang, Zhenghua Su, Guangxing Liang**

Y. Zhao, S. Chen, M. Ishaq, P. Fan, Z. Su, G. Liang

Shenzhen Key Laboratory of Advanced Thin Films and Applications Key Laboratory of Optoelectronic Devices and Systems, College of Physics and Optoelectronic Engineering

Shenzhen University, Shenzhen 518060, P. R. China.
E-mail: zhsu@szu.edu.cn (Prof. Su) and lgx@szu.edu.cn (Prof. Liang)

C. Yan

Sustainable Energy and Environment Thrust, Jiangmen Laboratory of Carbon Science and Technology, The Hong Kong University of Science and Technology (Guangzhou), Guangzhou, 510000, China

Y. Zhao, M. Cathelinaud, H. Ma, X. Zhang

CNRS, ISCR (Institut des Sciences Chimiques de Rennes), UMR 6226

Université de Rennes

Rennes F-35000, France

Content

Table S1. Summary of result REF, R1-R10, K_2S, K1-K10 samples derived from step profiler, XRD, XPS and EQE.

Sample	REF/K_2S	R1/K1	R2/K2	R3/K3	R4/K4	R5/K5	R6/K6	R7/K7	R8/K8	R9/K9	R10/K10
Thickness (μm)	1.2	1.1	1.0	0.9	0.8	0.7	0.6	0.5	0.4	0.3	0.2
(112) peak position	27.38/27.48	-	27.37/27.43	-	-	27.38/27.46	-	27.36/27.47	-	-	27.37/27.48
E_V (eV)	0.391/0.343	0.318/0.367	0.338/0.319	0.318/0.364	0.297/0.363	0.276/0.340	0.322/0.339	0.291/0.319	0.278/0.338	0.333/0.313	0.314/0.331
E_g (eV)	1.148/1.189	1.147/1.159	1.135/1.138	1.143/1.135	1.145/1.131	1.132/1.147	1.132/1.148	1.133/1.169	1.134/1.185	1.128/1.180	1.134/1.182

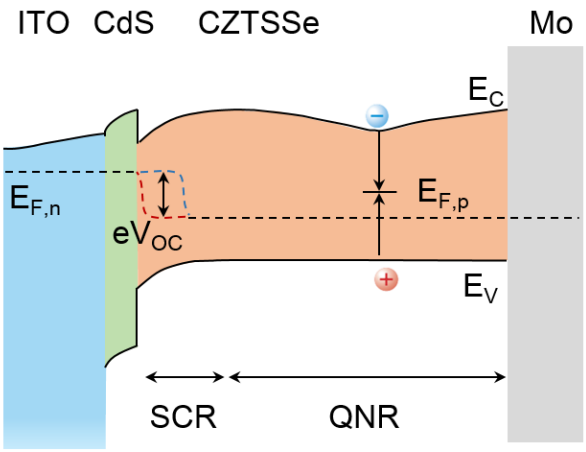

Figure S1. Schematic band diagram of an inappropriate double gradient band-gap with the front gradient starting from the quasi neutral region.

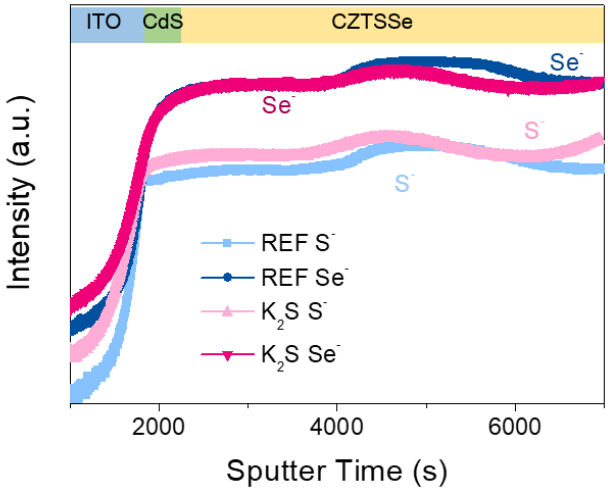

Figure S2. The depth distribution of S and Se in REF film and K_2S film detected by SIMS.

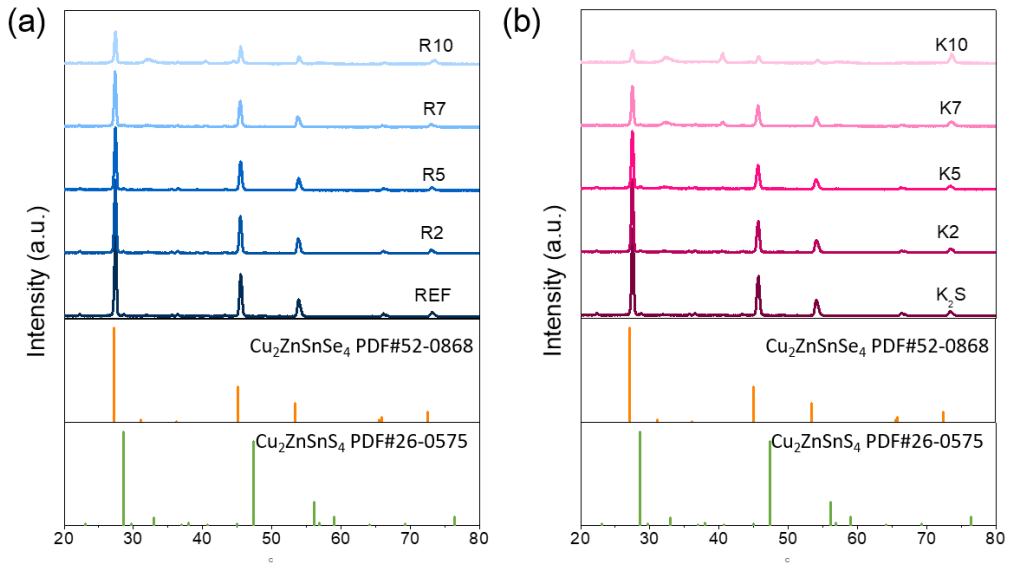

Figure S3. XRD of REF films (a) and K_2S films (b) with different thickness.

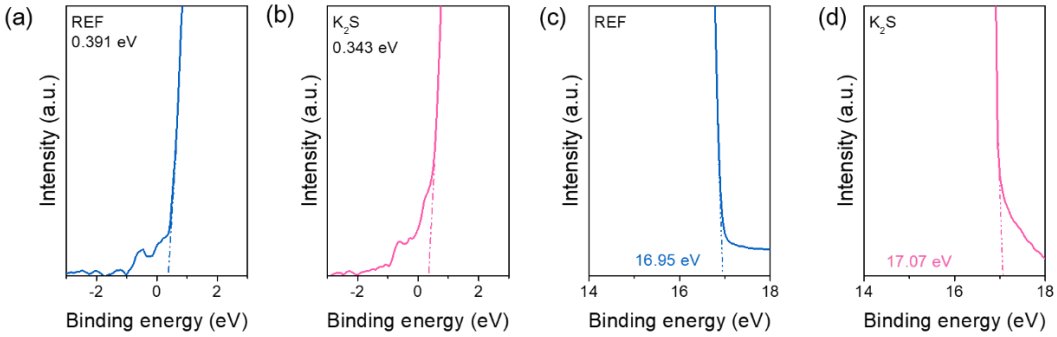

Figure S4. UPS spectra of REF film (a, c) and K_2S film (b, d).

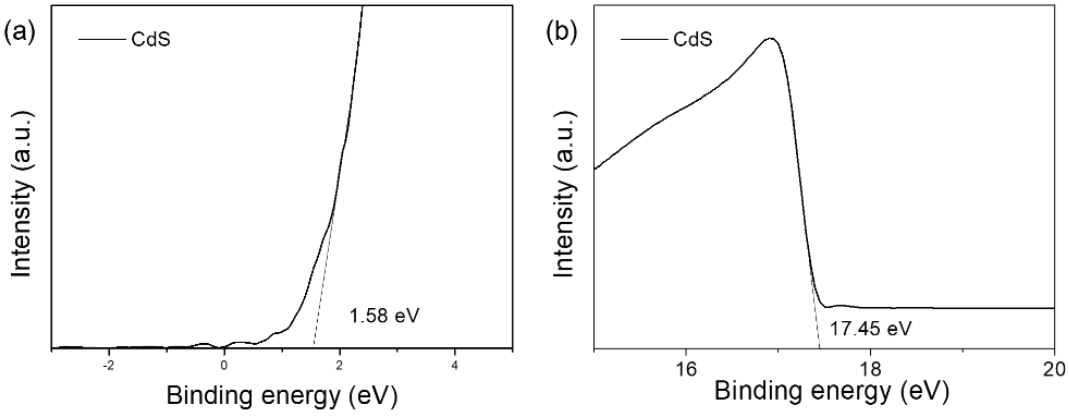

Figure S5. UPS spectra of CdS.

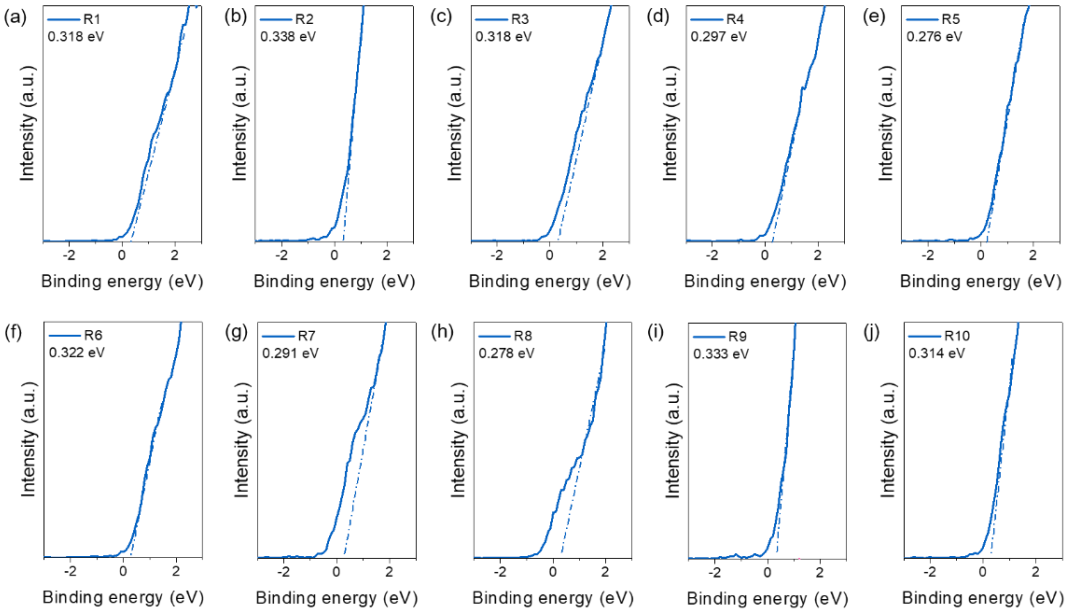

Figure S6. Valence band edge of R1-R10 films tested using XPS.

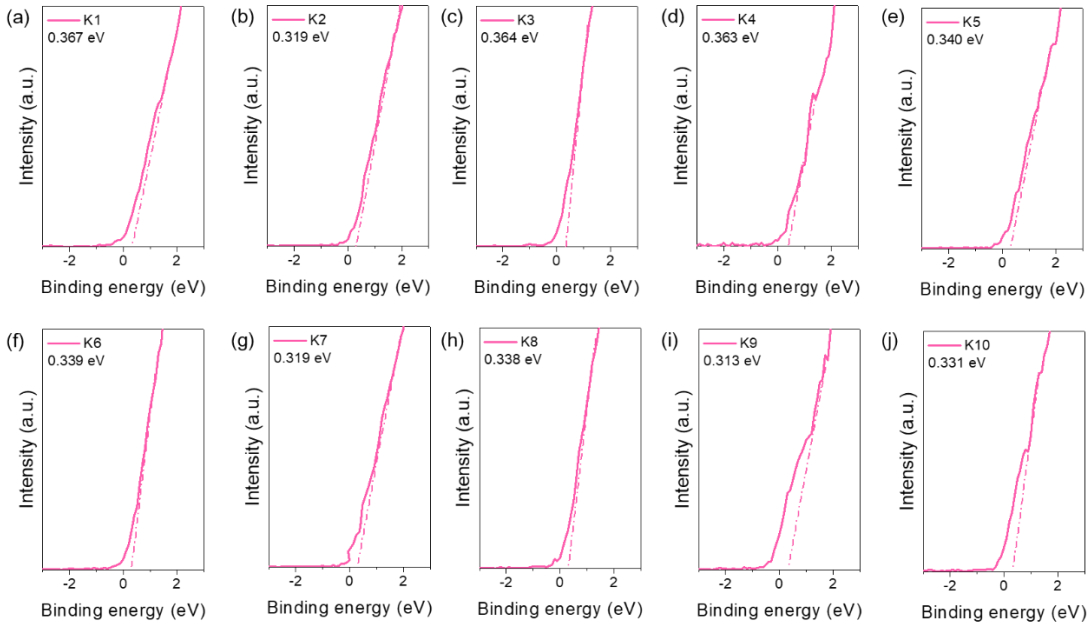

Figure S7. Valence band edge of K1-K10 films tested using XPS.

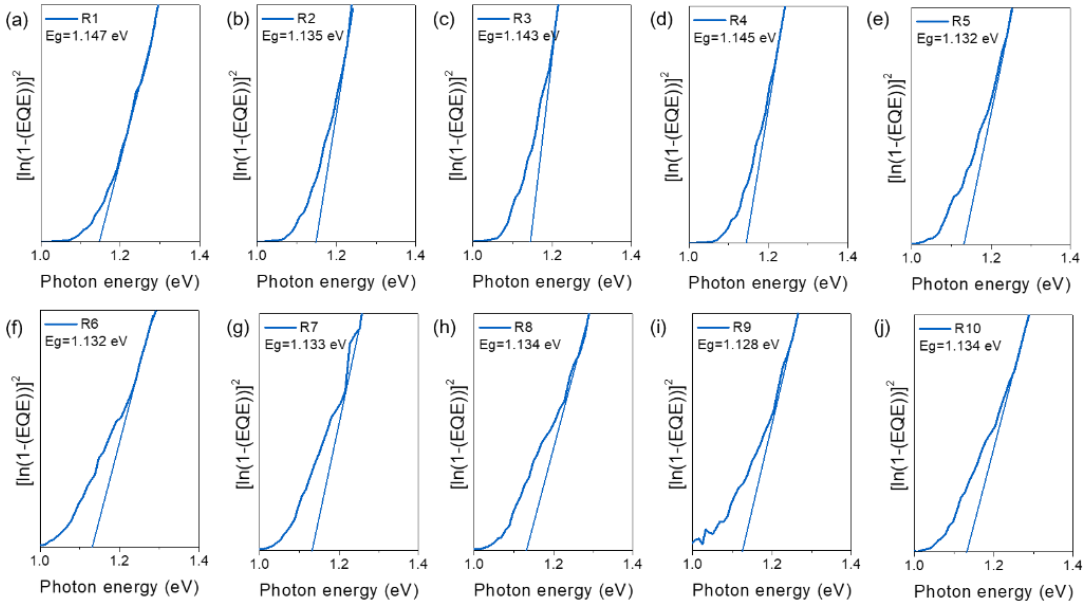

Figure S8. Band-gap of R1-R10 devices tested using EQE.

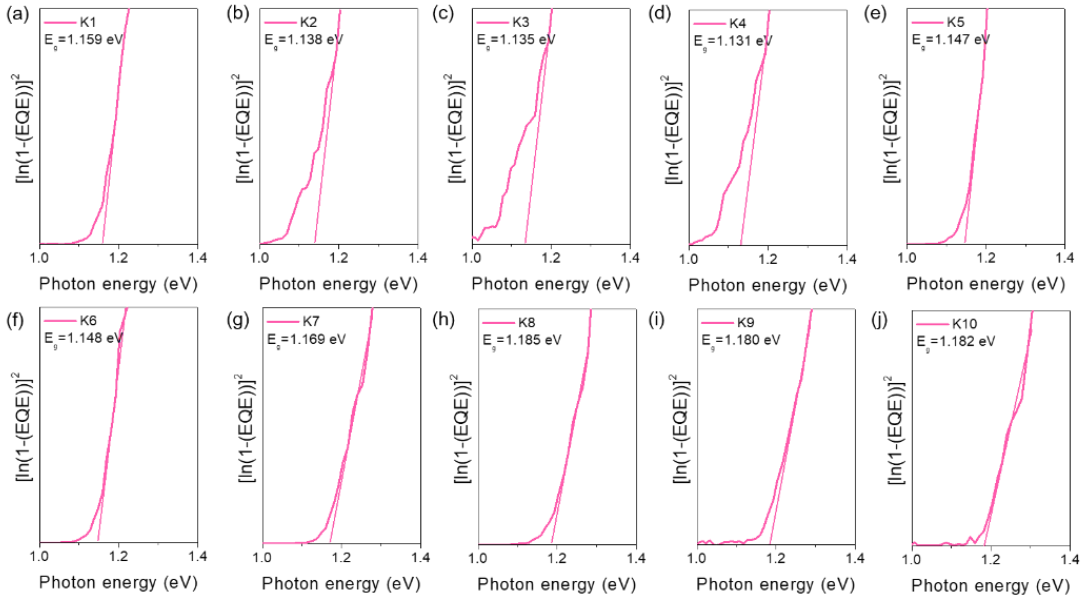

Figure S9. Band-gap of K1-K10 devices tested using EQE.

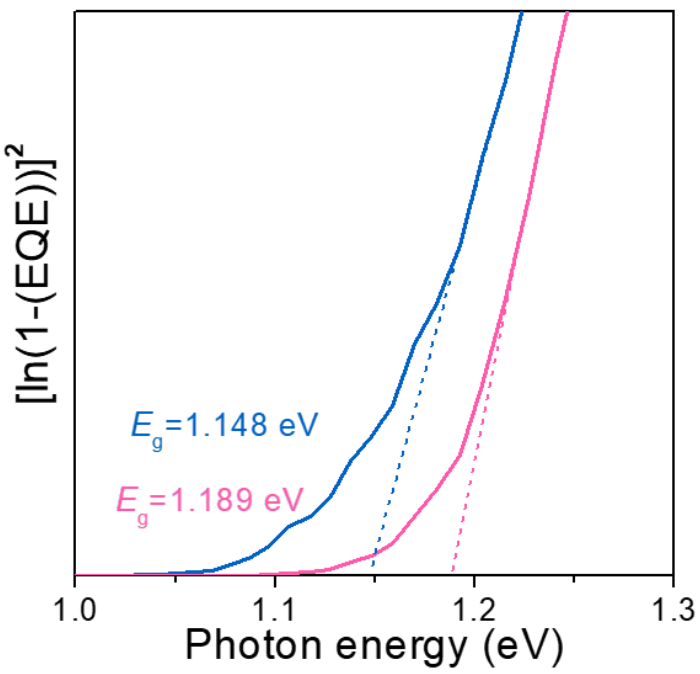

Figure S10. The extraction of band-gap from $[(-\ln(1-EQE))]^2$ versus E plots.

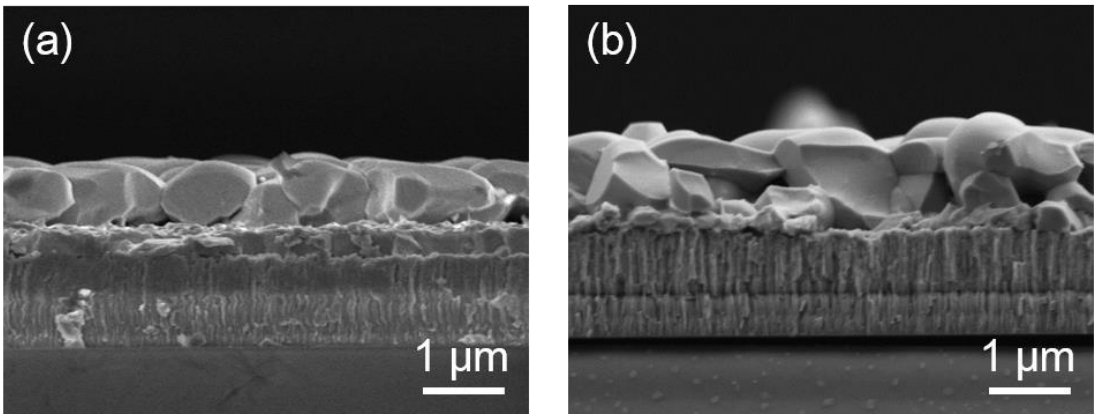

Figure S11. The cross sectional image of (a) REF film and (b) K_2S film.

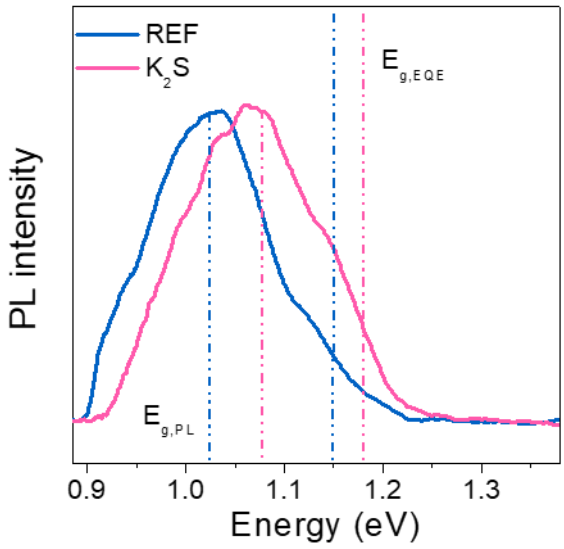

Figure S12. PL spectra of (a) REF film and (b) K_2S film.

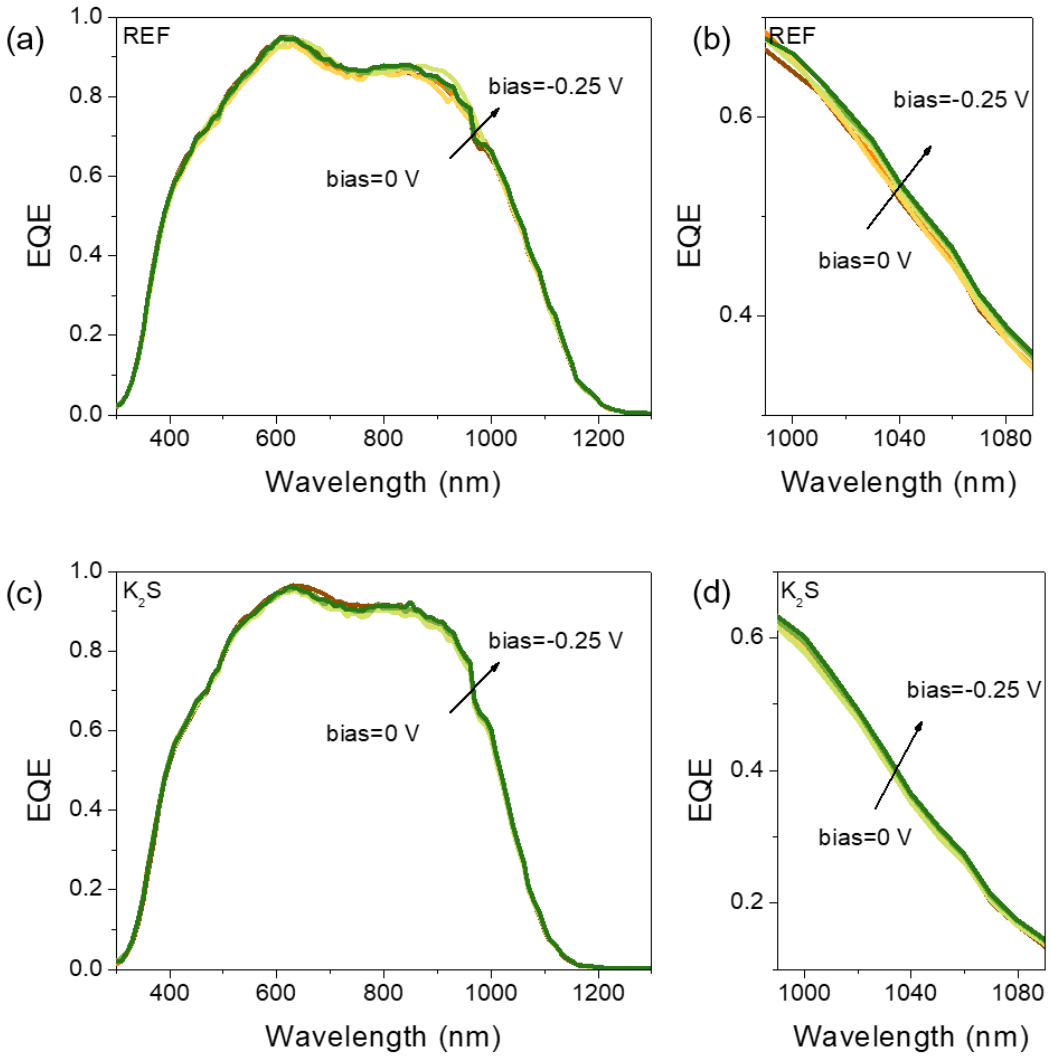

Figure S13. EQE characteristics for a bias range of approximately 0 to -0.25V for (a) REF device and (c) K_2S device. (b) and (d) are the partial enlargement of (a) and (c) respectively.

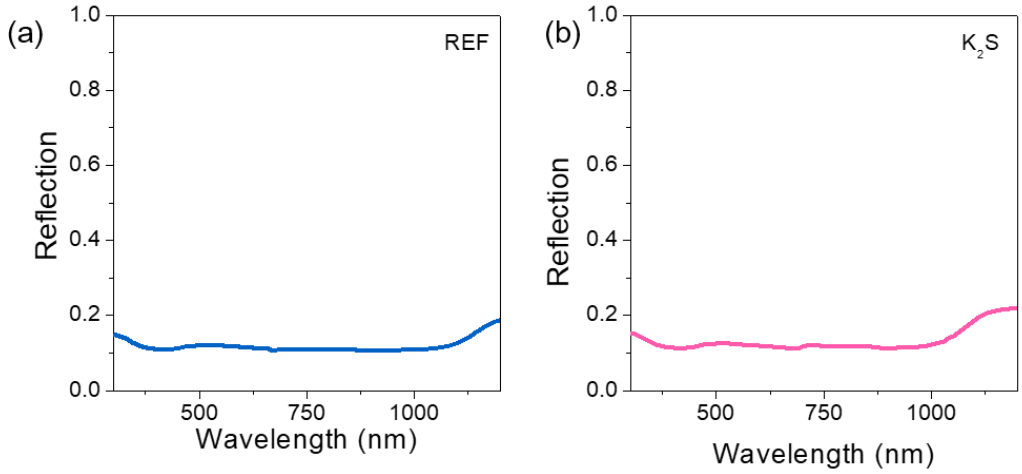

Figure S14. Reflection curves of (a) REF film and (b) K_2S film.

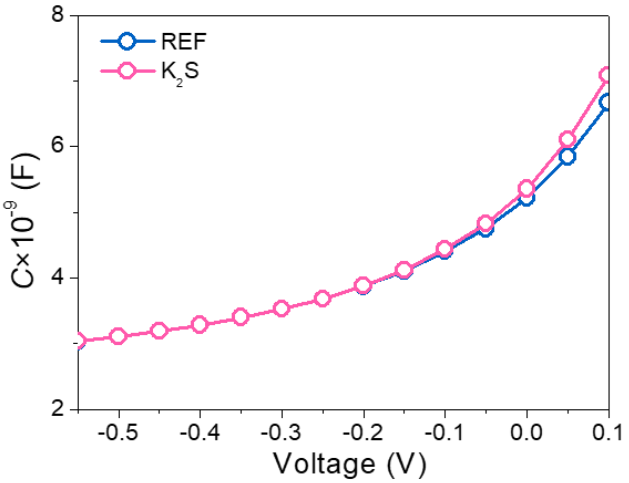

Figure S15. C-V curves of REF device and K_2S device.

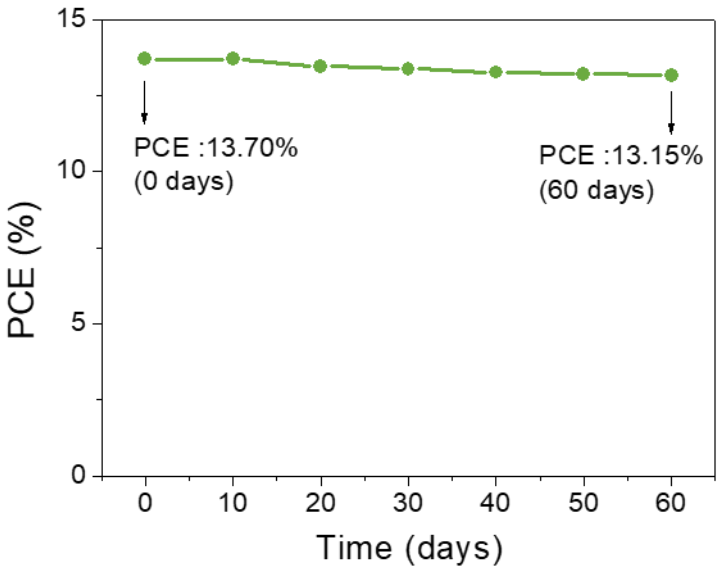

Figure S16 The PCE evolution of the Champion device after two months (60 days) of storage in an air environment, the device is not specially encapsulated.

Supplementary Note 1. Free carriers and interface defects density

The plots of N_{CV} and N_{DL} can be obtained by the following equations:

$$N_{CV} = \frac{C^3}{qA^2\varepsilon_0\varepsilon}\left(\frac{dC}{dV}\right)^{-1} \quad (1)$$

$$N_{DL} = -\frac{C_0^3}{2q\varepsilon_0\varepsilon A^2 C_1} \quad (2)$$

where ε and ε_0 are the dielectric constant of the CZTSSe and the vacuum dielectric constant, respectively. C, A, and q (1.60×10^{-19} C) are the measured capacitance, the active area of the solar cell, and elementary charge, respectively. C_0 and C_1 are two quadratic fitting parameters derived from the DLCP curves.[1, 2]

Supplementary Note 2. Minority carrier diffusion length

The bias-dependent EQE (**Figure S13**), reflectivity (**Figure S14**) and C-V measurements (**Figure S15**) were performed to investigate the L_d of REF and K_2S device. The calculation process and equations are shown in the supporting information. The calculation formulas of minority carrier diffusion length (L_d) were as follows:

$$IQE(\lambda, V) = \frac{EQE(\lambda,V)}{1-R(\lambda)} \quad (3)$$

$$IQE(\lambda, W_d) = 1 - \frac{exp(-\alpha(\lambda)W_d)}{1+\alpha(\lambda)L_d} \quad (4)$$

where EQE (λ,V) as function of wavelength (λ) and voltage bias (V) is measured, R(λ) is determined by the reflectivity as function of wavelength, The bias dependence of W_d was determined from the *C-V* measurement. The array of IQE (W_d, λ) data is fit to the analytic expression given by Equation (2) to extract a single L_d value and the absorption coefficient (α) at each λ.[3]

Supplementary Note 3. Deep level transient spectroscopy

The data in the DLTS are extracted from the current transient state at each temperature. The values of E_a and N_t can be calculated on an Arrhenius plot by linearly fitting the points near the DLTS peaks with the following equations:[4-6]

$$\ln(\tau * V_{th} * N_v) = ln(X_p\sigma) - \frac{E_a - E_v}{kT} \quad (5)$$

$$N_t = 2N_S\frac{\Delta C}{C_R} \quad (6)$$

$$V_{th} = \sqrt{\frac{3kT}{m_p^*}} \quad (7)$$

$$N_V = 2\left(\frac{2\pi m_p^* kT}{h^2}\right)^{\frac{3}{2}} \quad (8)$$

$$N_S = \frac{2C^2}{q\varepsilon A^2}(V + V_d) \quad (9)$$

Here, τ, V_{th}, N_V, σ and X_p are the emission time constant, carrier thermal rate, carrier effective density state, carrier capture cross section, and carrier entropy factor, respectively. And T, k, E_v, E_a, N_S, ΔC and C_R the temperature, Boltzmann's constant, valence band level, activation energy, capacitance at reverse-biased equilibrium, capacitance transient amplitude, and shallow defect density, respectively.

Reference

[1] Y. Zhao, S. Yuan, D. Kou, Z. Zhou, X. Wang, H. Xiao, Y. Deng, C. Cui, Q. Chang and S. Wu, *ACS Appl. Mater. Interfaces* **2020**, *12*, 12717-12726.

[2] R. Tang, S. Chen, Z. H. Zheng, Z. H. Su, J. T. Luo, P. Fan, X. H. Zhang, J. Tang and G. X. Liang, *Adv. Mater.* **2022**, *34*, e2109078.

[3] T. Gokmen, O. Gunawan and D. B. Mitzi, *J. Appl. Phys.* **2013**, *114*, 114511.

[4] S. Das, S. K. Chaudhuri, R. N. Bhattacharya and K. C. Mandal, *Appl. Phys. Lett.* **2014**, *104*, 192106.

[5] A. R. Daniel, K. Thomas and R. Uwe, *Advanced Characterization Techniques for Thin Film Solar Cells* Wiley, **2011**.

[6] R. Tang, X. Wang, W. Lian, J. Huang, Q. Wei, M. Huang, Y. Yin, C. Jiang, S. Yang, G. Xing, S. Chen, C. Zhu, X. Hao, M. A. Green and T. Chen, *Nat. Energy* **2020**, *5*, 587-595.